JGR Atmospheres

RESEARCH ARTICLE
10.1029/2024JD042024

Rapid Intensification of Hurricane Ian (2022) in High Shear

Alexander K. Nickerson[1], Jun A. Zhang[2], Robert H. Weisberg[1], and Yonggang Liu[1]

[1]College of Marine Science, University of South Florida, St. Petersburg, FL, USA, [2]NOAA/Atlantic Oceanographic and Meteorological Laboratory/Hurricane Research Division, and Cooperative Institute for Marine and Atmospheric Studies, University of Miami, Miami, FL, USA

Key Points:

- Hurricane Ian (2022) rapidly intensified while already a strong hurricane
- Intensification took place in unfavorable atmospheric conditions
- Anomalously warm waters on the West Florida Shelf enabled intensification

Correspondence to:

A. K. Nickerson,
anickerson@usf.edu

Citation:

Nickerson, A. K., Zhang, J. A., Weisberg, R. H., & Liu, Y. (2025). Rapid intensification of Hurricane Ian (2022) in high shear. *Journal of Geophysical Research: Atmospheres*, *130*, e2024JD042024. https://doi.org/10.1029/2024JD042024

Received 23 JUL 2024
Accepted 16 JUN 2025

Author Contributions:

Conceptualization: Jun A. Zhang
Data curation: Jun A. Zhang
Formal analysis: Alexander K. Nickerson, Jun A. Zhang, Robert H. Weisberg
Funding acquisition: Yonggang Liu
Methodology: Alexander K. Nickerson
Project administration: Yonggang Liu
Resources: Jun A. Zhang
Supervision: Jun A. Zhang, Robert H. Weisberg, Yonggang Liu
Writing – original draft: Alexander K. Nickerson, Robert H. Weisberg
Writing – review & editing: Alexander K. Nickerson, Robert H. Weisberg

Abstract Initially a Category 3 storm, Hurricane Ian (2022) rapidly intensified on the West Florida Shelf reaching Category 5 over the course of about 12 hr. Intensification occurred despite inhibiting factors such as high axial tilt, high vertical wind shear, low atmospheric moisture, and transit over a relatively shallow continental shelf. Using a high-resolution simulation of Hurricane Ian from the Hurricane Weather Research Forecasting (HWRF) model, we examine the factors that both hindered and supported rapid intensification (RI) by blending various methods. We show that an increase in diabatic heating in the eyewall led to an inward radial advection of momentum, seen in both the absolute angular momentum budget and in the azimuthal wind budget. Analysis of the moist static energy budget indicates that the substantial latent heat flux from the surface was enough to balance heat losses through storm outflow. For instance, surface latent heat fluxes exceeded 1,500 W m^{-2} on the West Florida Continental Shelf. As suggested by actual ocean temperature observations that substantially exceeded those in the HWRF simulation, the latent heating may have even been larger. Physical explanations for discrepancies between the simulated Hurricane Ian and observations are provided, particularly those pertaining to the coastal ocean at the time of Ian's passage. This research provides a comprehensive explanation of the RI of a hurricane using momentum budget analyses as part of a coupled air-sea analysis. Our findings demonstrate the importance of in situ oceanic air-sea measurements in evaluating the performance of coupled models, especially for hurricanes.

Plain Language Summary An already powerful Category 3 Hurricane Ian (2022) intensified by over 15 m s^{-1} in a 24 hr period over the shallow waters of the West Florida Continental Shelf. The rapid intensification occurred in an environment considered unfavorable for such a process. We analyzed the high-resolution forecast from an operational model to explain why Ian intensified. Using a variety of methods, we show that warmer-than-average waters on the shelf may have contributed to heat fluxes even higher than those predicted by the model, thereby fueling the storm.

1. Introduction

Forecasting rapid intensification (RI) in hurricanes poses significant challenges, resulting in models inaccurately predicting either the storm's intensity or its track (Bhatia et al., 2022). Such errors may lead to severe consequences including loss of life and financial damage, especially when the storm impacts a densely populated coastal region. Forecast models, even high-resolution models, have considerable errors with RI due to the complex multiscale processes that range from synoptic scales (>1,000 km) down to turbulent scales (<1 km).

Identifying the circumstances that may favor RI is difficult owing to the various factors that may be involved. Using the Statistical Hurricane Intensity Prediction Scheme (SHIPS), Kaplan et al. (2015) identified a set of environmental factors that favor RI: high precipitable water, low vertical wind shear, high upper-level divergence, and high ocean internal energy. These factors account for ∼25% of the forecast skill in RI scenarios, with the remaining ∼75% of the skill coming from inner core processes such as convection and turbulence. However, improved methods that correctly predict RI tend to increase the false-alarm ratio (Kaplan et al., 2010). Although improved models do have a modest impact upon decreasing the false-alarm ratio (J. A. Zhang, Cione, et al., 2017), Bhatia et al. (2022) show that evolving ocean and atmosphere states complicated the process beyond mere improvement in models. Recently, machine learning techniques have been shown to reduce the false-alarm ratio and to increase the detection of RI (e.g., Kim et al., 2024; Ko et al., 2023) despite performing similarly in non-RI scenarios.

A critical challenge in prediction is that some storms undergo RI despite lacking some of the previously mentioned conditions for RI. Recent examples include hurricanes Earl (2010), Edouard (2014), Harvey (2017),

and Dorian (2019) (e.g., Alvey et al., 2022; Montgomery et al., 2014; Potter et al., 2019; Rogers et al., 2015, 2016; Stevenson et al., 2014; Susca-Lopata et al., 2015; Zawislak et al., 2016). Extensive reconnaissance flights into Hurricane Earl expanded the understanding of RI (e.g., Smith et al., 2017) and improved forecast models (e.g., J. A. Zhang, Cione, et al., 2017; J. A. Zhang, Rogers, & Tallapragada, 2017; Wadler et al., 2018; J. A. Zhang & Rogers, 2019), yet there are many outstanding issues related to RI.

Beyond previously suggested indicators of RI, recent studies also suggest additional factors that may influence RI initiation. These include salinity stratification (Balaguru et al., 2020), the radial gradient of sea surface temperatures (SSTs) (J. A. Zhang et al., 2020; Z. Zhang et al., 2020), downdraft intensity (Wadler et al., 2018), latent heat flux (Richardson et al., 2022), combinations of diabatic heating (DH) and radial inflow of vorticity (Feng et al., 2024; Y. Li et al., 2021), topographic interactions (Alvey et al., 2022), advection of vorticity through vortex tilting (DesRosiers et al., 2022), ventilation (Fischer et al., 2023), precipitation symmetry (X. Chen, Xue, & Fang, 2018), moist static energy (MSE; X. Chen et al., 2019), wind field asymmetries (Nolan et al., 2023), vortex size (Huang & Ge, 2023), and even the phase of larger scale factors such as the Madden-Julian oscillation (Aberson & Kaplan, 2020). Eyewall contraction often precedes RI (e.g., Y. Li et al., 2021), but Qin et al. (2016) show that most storms reach a state, which they refer to as "steady," where eyewall contraction ceases, and in some cases, the eyewall even expands slightly near the completion of RI (H. Chen et al., 2011).

Atypical cases of RI are also noted, including those occurring in shallow water with low tropical cyclone heat potential (TCHP) (e.g., Potter et al., 2019), under high vertical tilt (e.g., Alvey & Hazelton, 2022; Alvey et al., 2022, 2025; DesRosiers & Bell, 2024; Feng et al., 2024; Ryglicki et al., 2021; Xie et al., 2024), in dry environments (Nam et al., 2023), and in moderate (e.g., Alvey & Hazelton, 2022; Alvey et al., 2022; Feng et al., 2024; Miyamoto & Nolan, 2018; Rios-Berrios et al., 2018; Rios-Berrios, 2020; Rogers et al., 2015; Ryglicki, Cossuth, et al., 2018; Ryglicki, Doyle, et al., 2018; Ryglicki et al., 2019; Wang et al., 2022) and high (e.g., Molinari & Vollaro, 2010; Nguyen & Molinari, 2012; Reasor & Eastin, 2012; Shelton & Molinari, 2009) wind shear. Some of these conditions have also been observed in general intensification and not just RI (e.g., Schecter, 2022, 2023; Yu et al., 2024). Hurricane Dorian (2019) underwent RI in a combination of moderate shear, high tilt, and low humidity (Alvey et al., 2022). As shear increases, the cases of RI that occur decreases (e.g., Nebylitsa et al., 2023), and shear even causes storms to weaken altogether (e.g., Gao & Wang, 2024). Among the environmental conditions, warm SST remains the only consistent requirement behind RI.

Judt et al. (2023) proposed a new paradigm in the form of two modes of RI, "sprint" and "marathon. The "marathon" mode, typically a gradual process over several days, occurs in low shear and high humidity (see their Figure 9a), while the "sprint" mode, a burst-like process over a period of about a day, occurs in moderate-to-high shear and low humidity. These analyses are limited to cases where the storms were initially classified as tropical storms or tropical depressions.

None of these studies explored a case such as Hurricane Ian (2022) in which RI occurred in an already powerful Category 3 storm (Saffir-Simpson scale). Kuo et al. (2019) examined Super Typhoon Haiyan, which underwent two RI cycles (31 m s^{-1} in 24 hr and 25 m s^{-1} in exactly 24 hr), but their model failed to capture two distinct RIs as occurred in Haiyan. In Ian, RI occurred in two stages, a process similar to Hurricane Opal (1995), which also underwent two stages of RI (Bosart et al., 2000) due to differing environmental conditions, much like Ian's intensification pause while passing over Cuba before the second period of RI that began over the West Florida Continental Shelf (WFS).

This paper focuses on Hurricane Ian and its RI over the WFS. Section 2 describes the model used for the analysis of the storm and the thermodynamic, dynamic, and oceanic processes and variables examined. Section 3 contains an overview of Hurricane Ian and its environment. Section 4 describes and discusses the analysis findings, and Section 5 draws conclusions from the analyses. Through these analyses, we aim to explain how a hurricane can undergo RI in water that is relatively shallow (initially less than 100 m deep and then less than 50 m deep).

2. Data and Methods

2.1. Model Data

We use the Hurricane Weather Research Forecasting (HWRF) model to analyze Ian's RI. The HWRF version 4.0a model (Biswas, Carson, et al., 2018) features a triple-nested grid on a storm-following coordinate with grid sizes of 13.5, 4.5, and 1.5 km. The 1.5-km grid is a 9° × 9° storm-following coordinate system with 46 vertical levels

that range from 1,000 hPa at the base level to 2 hPa at the top of the model domain. Where possible, we use the 1 hr diagnostic output file, which includes many key variables (e.g., SST, sea level pressure).

The atmospheric model is coupled with the Princeton Ocean Model (POM) to allow air-sea exchanges, leading to more accurate estimations of air-sea enthalpy fluxes. The POM has a domain encompassing the entire tropical North Atlantic basin at approximately 9-km grid spacing in the horizontal and 40 sigma coordinate points in the vertical.

The HWRF model is written in pressure coordinates with terms of $\omega\partial/\partial p$ and the height $Z = Z(\alpha,\varphi,p)$, where α is the longitude, φ is the latitude, and p is the pressure. In this study, the three-dimensional atmospheric variables will be viewed in cylindrical, polar coordinates, with r the radius, λ the polar angle, p the pressure coordinate, u the radial wind speed (positive is outward from the center), and υ the azimuthal wind speed (positive is cyclonic). At each layer of the model, the storm center is estimated as the local wind minimum in the eye of the storm.

SHIPS (DeMaria & Kaplan, 1994; https://rammb2.cira.colostate.edu/research/tropical-cyclones/ships) provides estimates of relative humidity, storm shear, and precipitable water, making it a vital component of forecast ensembles suites (DeMaria et al., 2022). The 850–200-hPa shear and relative humidity were originally spatially averaged over 200–800-km from the storm center (DeMaria et al., 2005), but more recent versions of SHIPS use 0–500-km after removing the storm vortex (Kaplan et al., 2010, 2015). Rios-Berrios et al. (2024) correctly point out that using a spatial average in this region does not necessary represent what is happening in the storm core.

The HWRF simulation we use is from the operational run initialized at 1800 UTC 27 September 2022. This run corresponds to the first forecast point following Ian's egress from Cuba and is less than 12 hr before Ian traverses the shelf break on the WFS. The model output time step is 3 hr for the 1.5-km domain and 1 hr for the diagnostic file. The meridional and zonal winds were passed to the ocean via the model coupler, and from the ocean model, the latent heat fluxes were calculated and returned to the atmosphere. The model vortex was initialized using the previous 6-hr forecast and corrected using the storm size, location, and intensity. Model domains received their initial fields from the Global Forecast System, which was then interpolated onto the inner domain grids. Observational data used in initializing the model include dropsondes, reconnaissance, and satellite observations. Further details about the operational HWRF can be found in the model documentation (Biswas, Abarca, et al., 2018).

2.2. Oceanic Data

Tropical cyclone heat potential (TCHP) was first proposed by Whitaker (1967) to account for mixed layer depths and later popularized by Leipper and Volgenau (1972). TCHP is defined as

$$\mathrm{TCHP} = c_p \int_{z=0}^{z(T=26^\circ C)} \rho_i (T_i - 26)\, dz, \tag{1}$$

where c_p is the specific heat of water ($\sim$3,850 J kg^{-1} °C^{-1}), $z = 0$ at the surface of the water, z ($T = 26$°C) is the depth of the 26°C isotherm, T_i is the temperature of the parcel at level i, ρ_i is the density of a water parcel at level i, and dz is the height of the water parcel level i. We also examine the air-sea enthalpy flux (the sum of the surface latent and sensible heat fluxes).

We supplement the model output with in situ observations from four Coastal Ocean Monitoring and Prediction System (COMPS) stations located on the WFS. These strategically positioned stations are located along different isobaths of the WFS in order to best capture the various processes first described in detail by Z. Li and Weisberg (1999a, 1999b) and elaborated by Weisberg et al. (2001, 2009, 2015), Weisberg and He (2003) with the added context of the Gulf of Mexico Loop Current in relation to the WFS topography by Liu et al. (2016). We compare the POM temperatures to the in situ observations in order to evaluate the HWRF simulation's performance on the WFS. The COMPS SSTs and the NOAA best track use observations; all other analyses we perform use the HWRF simulation of Hurricane Ian.

2.3. Moist Static Energy

Moist static energy can be considered a state variable since it is defined in terms of three state variables: temperature (T), height (z), and specific humidity (q). The MSE (h) is defined as

$$h = c_p T + gz + L_v q, \tag{2}$$

where c_p is the specific heat of dry air at a constant pressure (~1,004.7 J kg^{-1} K^{-1}), g is the gravitational constant (~9.81 m s^{-2}), and L_v is the latent heat of vapourization for liquid water (~2.5 × 106 J kg^{-1}). The first term on the right side of Equation 2 is the enthalpy at a constant volume, the second term is the geopotential energy, and the last term is the latent heating. Also of importance is the moist enthalpy, k, defined as

$$k = c_P T + L_v q. \tag{3}$$

MSE is widely used in the tropics, including studies on the intertropical convergence zone (e.g., Neelin & Held, 1987), the Madden-Julian oscillation (e.g., Sobel et al., 2014), and tropical cyclones (e.g., Emanuel, 2018; Juračič & Raymond, 2016), because its column integral is conserved. Using the moist enthalpy in the local change term gives better closure to the MSE budget (Neelin, 2007), as has been also shown to apply in HWRF (X. Chen et al., 2019) and the advanced HWRF (Fischer et al., 2023).

2.4. Diabatic Heating

A critical part of the spin-up mechanism is the increase in DH of the core of the storm. DH drives the inward radial advection of absolute angular momentum (AAM) (Ooyama, 1982) that leads to increasing tangential winds. DH of a system is simply defined (following Kuo et al., 2019) as the material derivative of the potential temperature:

$$Q = \frac{D\theta}{Dt} = \frac{\partial\theta}{\partial t} + u\frac{\partial\theta}{\partial r} + \frac{v}{r}\frac{\partial\theta}{\partial\lambda} + \omega\frac{\partial\theta}{\partial p}, \tag{4}$$

where θ is the potential temperature. Following a Reynolds decomposition Equation 4 can be azimuthally averaged to give

$$\overline{Q} = \frac{D\overline{\theta}}{Dt} = \frac{\partial\overline{\theta}}{\partial t} + \overline{u}\frac{\partial\overline{\theta}}{\partial r} + \overline{\omega}\frac{\partial\overline{\theta}}{\partial p} + \overline{u'\frac{\partial\theta'}{\partial r}} + \overline{\omega'\frac{\partial\theta'}{\partial p}}, \tag{5}$$

with the overbars denoting azimuthal means and the primes denoting departures from the mean.

2.5. Absolute Angular Momentum

The AAM is the second part of the spin-up of hurricanes (e.g., Persing et al., 2013; Montgomery et al., 2014; Smith et al., 2017; J. A. Zhang & Rogers, 2019; sources within these papers). The AAM (M) is defined as

$$M = rv + \frac{1}{2}fr^2, \tag{6}$$

where M is the AAM, r is the radius, v is the azimuthal wind speed, and f is the local planetary vorticity. In hurricanes, as in the case of J. A. Zhang and Rogers (2019), the azimuthally averaged AAM balance provides a simple view of spin-up. The AAM balance is given by

$$\frac{\partial M}{\partial t} = -u\frac{\partial M}{\partial r} - \frac{v}{r}\frac{\partial M}{\partial\lambda} - \omega\frac{\partial M}{\partial p} + F_r, \tag{7}$$

where Fr represents the model residual. The spin-up mechanism is seen, following Smith et al. (2017), via the azimuthally averaged AAM budget,

$$\frac{\partial \overline{M}}{\partial t} = -\overline{u}\frac{\partial \overline{M}}{\partial r} - \overline{\omega}\frac{\partial \overline{M}}{\partial p} - \overline{u'\frac{\partial M'}{\partial r}} - \overline{\omega'\frac{\partial M'}{\partial p}} + F_r. \quad (8)$$

2.6. Wind Component Balances

Due to the limited use of AAM in the boundary layer, Persing et al. (2013), Montgomery et al. (2014), and Smith et al. (2017) demonstrated increased accuracy by analyzing the budget of the azimuthal wind. The planetary boundary layer height is that from the HWRF model output, determined via the virtual temperature profile, the wind speed at the top of the layer, and the critical Richardson number. In highly sheared or tilted storms, Nolan and McGauley (2012) suggested that momentum evaluation (e.g., $\partial\overline{v}/\partial t$) using actual wind analyses may not be effective. The agradient wind (v_a), the difference between the tangential wind speed and the gradient wind, is derived from the gradient wind (v_g) by solving the quadratic equation:

$$\frac{1}{r}v_g^2 + fv_g + \left(-g\frac{\partial Z}{\partial r}\right) = 0 \quad (9)$$

for v_g and subtracting v_g from v. If $O(v_a) = O(v_g)$, then it is likely that the budget of the azimuthal wind will be more reliable than the budget of the AAM. We will show that $O(v_a) = O(v_g)$ in Section 4.3. The budgets for the individual wind components are

$$\frac{\partial v}{\partial t} = -u\frac{\partial v}{\partial r} - \frac{v}{r}\frac{\partial v}{\partial \lambda} - \omega\frac{\partial v}{\partial p} - \left(f + \frac{v}{r}\right)u - g\frac{1}{r}\frac{\partial Z}{\partial \lambda} + D_v \quad (10)$$

$$\frac{\partial u}{\partial t} = -u\frac{\partial u}{\partial r} - \frac{v}{r}\frac{\partial u}{\partial \lambda} - \omega\frac{\partial u}{\partial p} + \left(f + \frac{v}{r}\right)v - g\frac{\partial Z}{\partial r} + D_u \quad (11)$$

Taking the azimuthal mean of the above equations gives

$$\frac{\partial \overline{v}}{\partial t} = -\overline{u}\left(\overline{f+\zeta}\right) - \overline{\omega}\frac{\partial \overline{v}}{\partial p} - \overline{u'\,\zeta'} - \overline{\omega'\frac{\partial v'}{\partial p}} + \left(\overline{-g\frac{1}{r}\frac{\partial Z'}{\partial \lambda}}\right) + \overline{D_{vh}} + \overline{D_{vp}} \quad (12)$$

$$\frac{\partial \overline{u}}{\partial t} = -\overline{u}\frac{\partial \overline{u}}{\partial r} - \overline{\omega}\frac{\partial \overline{u}}{\partial p} + \left[\left(f + \frac{\overline{v}}{r}\right)\overline{v} - g\frac{\partial \overline{Z}}{\partial r}\right] - \left(\overline{u'\frac{\partial u'}{\partial r} + \frac{v'}{r}\frac{\partial u'}{\partial \lambda}}\right) - \overline{\omega'\frac{\partial u'}{\partial p}} + \left(\overline{-g\frac{\partial Z'}{\partial r} + \frac{v'^2}{r}}\right) + \overline{D_{uh}} + \overline{D_{up}}, \quad (13)$$

where g is the gravitational constant, Z is the atmospheric height, ζ is the vertical component of the relative vorticity, and the D terms represent diffusive tendencies. The terms that include the derivatives of Z represent gradient forces, and the Z' terms represent agradient forces. Unlike the AAM budget, the horizontal wind budgets should balance in the boundary layer. Above the boundary layer, the winds are typically in approximate gradient wind balance, but this does not hold true in the strong inflow region of the boundary layer. For instance, in Hurricane Ian, it is expected that supergradient winds will be found, similar to those found in Hurricane Earl in 2010 (Montgomery et al., 2014).

3. Storm Evolution

A disturbance formed over the tropical waters of the Caribbean Sea on 22 September 2022, developing into Tropical Storm Ian the following day. The system initially moved westward before turning northward and intensifying into a hurricane. Ian underwent its first RI cycle, strengthening 20 m s^{-1} in 24 hr before making landfall over western Cuba. Maintaining its Category 3 status while traversing Cuba, Ian then moved onto the WFS. Once on the WFS, Ian again underwent RI, strengthening to a Category 5 hurricane before making landfall over Lee County, Florida (Figure 1a). Actual landfall happened ~70 km south of the HWRF predicted location.

During Ian's second period of RI, beginning at 0000 UTC 28 September 2022, Ian's wind speed increased by ~15 m s^{-1} in 12 hr (Figure 1b), with the HWRF simulation predicting an increase of ~12 m s^{-1} over the same period. As seen from SHIPS output, RI took place despite the presence of high shear (10–15 m s^{-1}, Figure 1c), which increased throughout the forecast period, and relative dry conditions (60%–70% relative humidity,

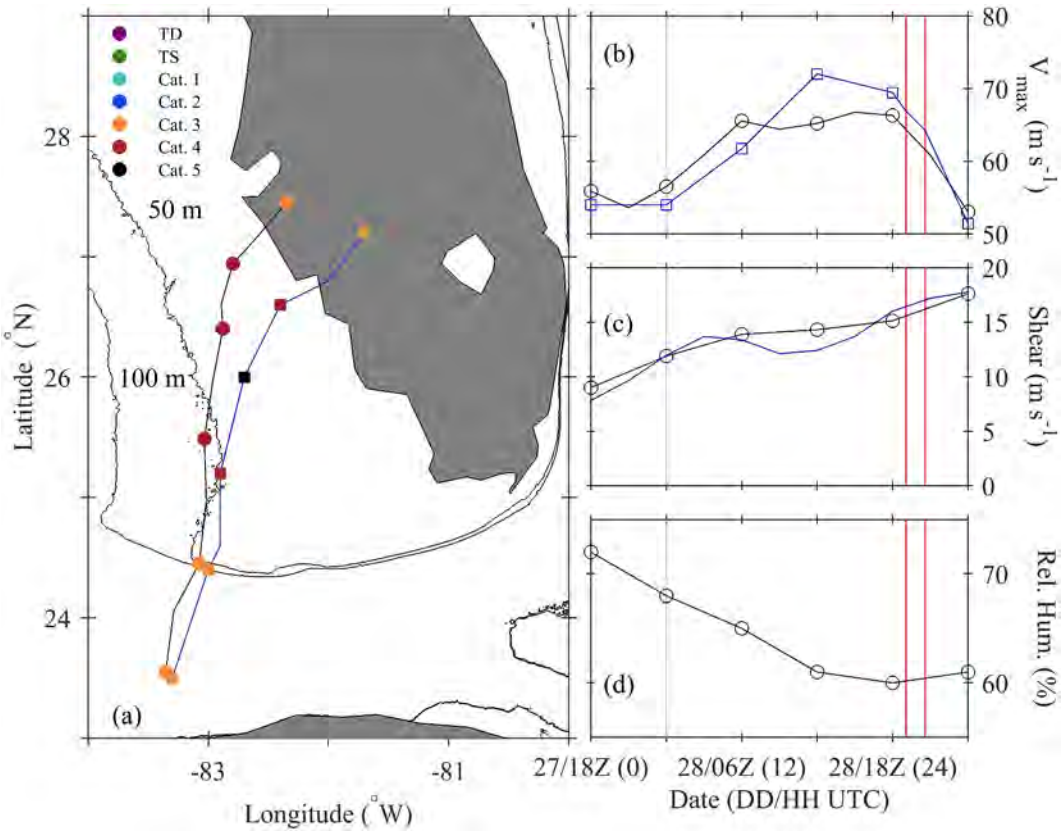

Figure 1. (a) Storm track (black line, circles) and Hurricane Weather Research Forecasting (HWRF) forecast track (blue line, squares) of Hurricane Ian for the time between model initialization and landfall. Included are the 50 and 100 m isobaths of the West Florida Shelf. (b) Observed (black) and HWRF forecast (blue) maximum wind speed in m s^{-1}. (c) Statistical Hurricane Intensity Prediction Scheme (SHIPS) (black) and HWRF (blue) 850–200-hPa wind shear magnitude in m s^{-1}. (d) SHIPS 850 to 700-hPa average relative humidity for 200–800 km from the storm center. The gray vertical line represents the initialization of rapid intensification; the red lines represent Ian's landfalls in Cayo Costa and at Pirate harbor.

Figure 1d), which decreased over the same time. Moreover, at the start of RI, the storm was tilted (900–300 hPa, Figure 2a) downshear (as in Yu et al., 2023), with the magnitude of the tilt decreasing during RI despite shear increasing to 15 m s^{-1} during the simulation, conditions that represent about 1% of all RI cases (see Nebylitsa et al., 2023; Figure 5).

The tilt consistently remained southward (Figure 2b), and the departure of the tilt (which we define as the angle between the tilt and a vertical line up from 900 hPa) decreased along with the tilt magnitude. When comparing to studies, such as Alvey et al. (2022, 2025), tilting was due to persistent shear, which was consistently from the northeast (Figure 2c). This realignment of the lower and upper level vortices is consistent with Fischer et al. (2022, 2024) and was previously hypothesized to be necessary for intensification (Alvey et al., 2020; X. Chen, Wang, et al., 2018; Rios-Berrios et al., 2018; Rogers et al., 2020; Schecter & Menelaou, 2020). The radius of maximum wind (Rmw) decreased from nearly 50 km to under 30 km during RI (Figure 3a), while convective activity, indicated by cloudbursts (points within 200 km of the storm center and with a vertical velocity greater than 3 m s^{-1}), increased during the period of intensification and decreased when the storm began interacting with the Florida Peninsula (Figure 3b).

Previous studies linked increased cloudbursts to intensification (e.g., H. Chen & Gopalakrishnan, 2015; Nolan et al., 2007; Rogers et al., 2013, 2015; Vigh & Schubert, 2009), and the last of these studies specifically showed that cloudbursts, especially in the downshear left and upshear left regions, can lead to central pressure drops as part of RI. Here, cloudbursts are seen in both of the downshear quadrants (as in Schecter, 2024) as well as the upshear left quadrants, much like Alvey et al. (2020) found for pre-RI convection. In the case of sheared storms, Huang and Ge (2023) found that strong outflow and convection in the upshear left side can offset the shear, thus

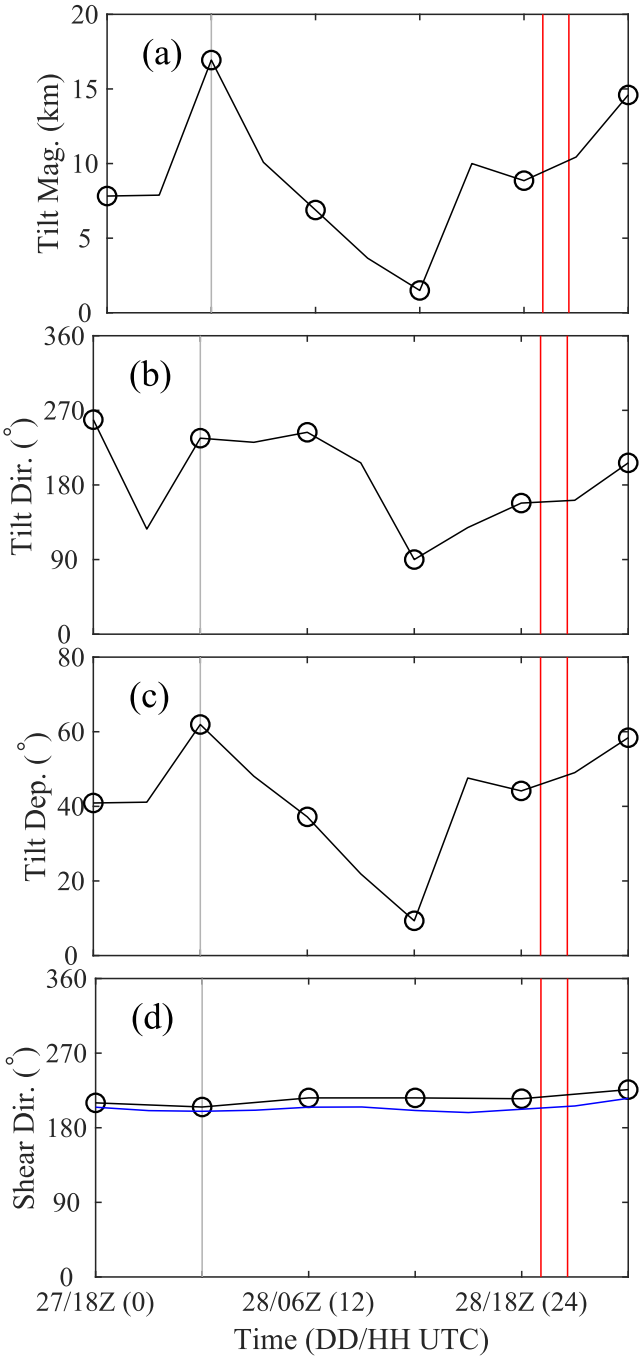

Figure 2. (a) The magnitude of the 900–300-hPa storm tilt in km; (b) the angle of the storm tilt (black); (c) the angle of the tilt departure from the vertical; (d) the angle of the vertical wind shear from Statistical Hurricane Intensity Prediction Scheme (black) and Hurricane Weather Research Forecasting (HWRF) (blue). The direction of the tilt is based on 0° being toward the north and 180° being toward the south. Plots (a)–(c) come from HWRF. The vertical lines are as in Figure 1.

allowing intensification to occur. Alvey and Hazelton (2022) show RI being preceded by both realignment and increased convection in the early morning hours, but Ian's RI is accompanied by realignment and most rapid during the night, which favors intensification due to destabilization of the atmosphere (Dunion et al., 2019; Tang & Zhang, 2016; J. A. Zhang et al., 2020; Z. Zhang et al., 2020). Given such adverse kinematics, something else must have influenced Ian's RI over the WFS.

At this point, it is important to digress regarding the observed Ian track as compared with the track of the HWRF simulation used here for analysis. Note that these two tracks are very similar over the RI time period. Only after RI did the tracks begin to deviate, with the simulated track showing landfall farther north of the observed track. We will return to this point later when we introduce the simulated and observed sea surface and subsurface temperatures in Figures 7 and 8, which will reinforce our analyses.

The kinematics of Ian as it underwent RI are revealed in the six-hourly snapshots of the HWRF simulated, azimuthally averaged, radial, azimuthal, and vertical components of wind as functions of radial distance from the storm center and height, shown in Figure 4. During the RI process, the radial wind maximum moves inward and increases in magnitude, while the vertical updraft in the eyewall becomes stronger and more pronounced, as does the adjacent interior downdraft. These changes are accompanied by an increase in the azimuthal wind and a stronger outflow at the top of the storm. The initial dry pocket at the top of the eye (8–12 km above the surface, Figure 5) spreads vertically to 2 km above the surface as the eyewall becomes more pronounced and forms a dry slot at ∼10 km. The evolving dry slot eventually grows from the top of the storm to the bottom as a pronounced, well-defined eye forms, contrary to the expected weakening associated with such high shear (e.g., Frank & Ritchie, 2001).

Figure 6 illustrates the distribution of the cloudbursts and the equivalent potential temperature (θ_e, calculated relative to 1,000-hPa as in Bolton, 1980, Equation 38). The primary cloudburst band becomes more defined, wider, and concentrated (Figure 6) along the eyewall. At the same time, the eye (e.g., θ_e) becomes more concentrated and well-defined, indicating a more organized and intense storm structure. Carstens et al. (2024) showed that θ_e in the upshear right region is most important for intensification, but in Ian, there appears to be a fairly symmetric distribution of heat. At least kinematically, the HWRF simulation seems to have captured the structure of Ian as it intensified and eventually started to dissipate once land effects came into play. The plots of the modeled radial storm structure at 850 mb and the normalized azimuthal wind profiles from reconnaissance flights (Figure 4) show slight variations.

4. Storm Analysis

4.1. Oceanographic Factors

The ocean environment in which RI initiated was sufficiently warm despite the water on the WFS being shallow (<100 m). The RI began as the storm straddled the escarpment along the Straits of Florida (Figure 7, top row). This region had TCHP values over 100 kJ cm^{-2} and continued over areas where the TCHP was still above 60 kJ cm^{-2} Mainelli et al. (2008, and sources therein) showed that the TCHP is a strong indicator of RI, especially when it exceeds 60 kJ cm^{-2}, and also linked TCHP to Category 5 hurricanes. The model output indicates TCHP is above 60 kJ cm^{-2} for both the observed and HWRF simulated tracks.

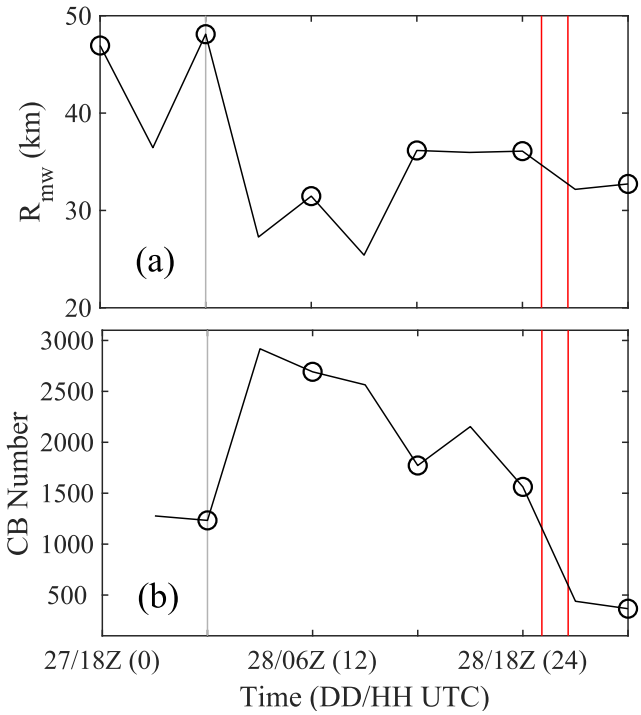

Figure 3. Hurricane Weather Research Forecasting (a) radius of maximum wind (km) and (b) cloudburst number. The vertical lines are as in Figure 1.

The air-sea enthalpy flux, dominated by the latent heat flux term, was high and sustained throughout the model run (Figure 7, middle row). SSTs remained above 28°C during the RI period (Figure 7, bottom row), ensuring a steady energy supply for its 24 hr over the WFS. Potter et al. (2019) similarly showed that Hurricane Harvey (2017) intensified despite having TCHP values that were below the threshold, demonstrating another example of RI over a shallow escarpment.

The HWRF/POM-simulated WFS SST, however, is cooler than the observed SST from three of the four moored buoy stations (Figure 8). Only at C10 (Figure 8a), which received the least direct impact from Ian, is the SST initially warmer. The warmer SSTs at the other three stations were more favorable for RI, giving a possible explanation for why the simulated hurricane was less intense than the observed hurricane. The initial simulated and observed SSTs were similar at C12 (b), but the SST decrease was greater in the simulation than in the observations due to the actual track being more southerly. At C13 (c) and C22 (d), both the simulated and the observed hurricanes passed directly over the moorings, and the simulated SSTs were cooler than the observed SSTs, peaking at 0.5°C at C12, 1.1°C at C13, and 0.9°C at C22. The modeled SST decrease begins earlier at C22 than in the observations. After the passage of Ian, the temperature decreased approximately 3°C at C12 (both at the surface and at depth) and C22 but decreased only 2°C at C10 and C13.

At the model initialization, there is a period of rebound for the modeled SSTs at C10 and C12. Thus, the modeled SSTs are either erroneous (as at C10 and C12) or too low (as at C13 and C22) at the beginning of the simulation. POM SSTs, which are used to determine the latent heat flux, remained below the observed values at all times. Consequently, assuming all other variables remained constant, the air-sea enthalpy flux into Ian was higher than predicted by the simulation. Liu et al. (2025) provide the oceanographic explanation for why the WFS waters were anomalously warm, the importance of deeper water, and hence what helped facilitate Ian's RI. When including more observations than just SSTs, the discrepancies become more evident.

Although differences exist between the modeled track and the actual track (and thus any differences in the modeled and actual storm environments), we can refer to Equations 3 and 4 from the Sorinas et al. (2023) study to make inferences about the latent and sensible heat fluxes. From Figure 8, we can generally conclude that the HWRF SSTs are consistently up to ∼1°C lower than observed SSTs at the four buoys, and likewise, the modeled air temperatures are up to 3°C higher than the in situ values, as seen in Figure 8. During RI, these values peak at 2.5°C at C10, 1.6°C at C12, 3.2°C at C13, and 1.6°C at C22. Relative humidity observations are likewise lower than modeled values. During the times that the modeled and actual storm tracks are similar, the wind speeds are also similar, although C22 suffered an instrument failure early in the RI period.

Using C13 for an example and Equations 3 and 4 from Sorinas et al. (2023), we can make estimates of the differences in the sensible and latent heat fluxes. Since ρ_a, L_e, c_p, C_l, and C_s are all constants or approximately constant, and the value of W_{spd} is approximately the same in both the simulated and actual conditions from model initialization until the tracks begin to diverge at 0300 UTC 28 September 2022, we only need to consider Δq, the difference between specific humidity and saturation specific humidity, and ΔT, the temperature gradient from the surface to the air. For consistency across comparisons, we compute both specific humidities from the air pressure, air temperature, and relative humidity for the HWRF output and the COMPS stations using the equations from Salby (1996) and Wallace and Hobbs (1977). By using the observed temperature for computing the specific humidity, we account for differences in the modeled and observed air temperature and dew point.

When computed, according to the data shown in Figure 8, Δq at C10 cannot be compared because of the saturation of the modeled atmosphere; at C12, Δq in the observations is larger by a factor between 1.25 and 2; at C13, saturation of the modeled atmosphere hinders the comparison between the model and observations, but the observed Δq is larger by a factor of 1–2; and at C22, saturation of the model again is the prevailing factor. From

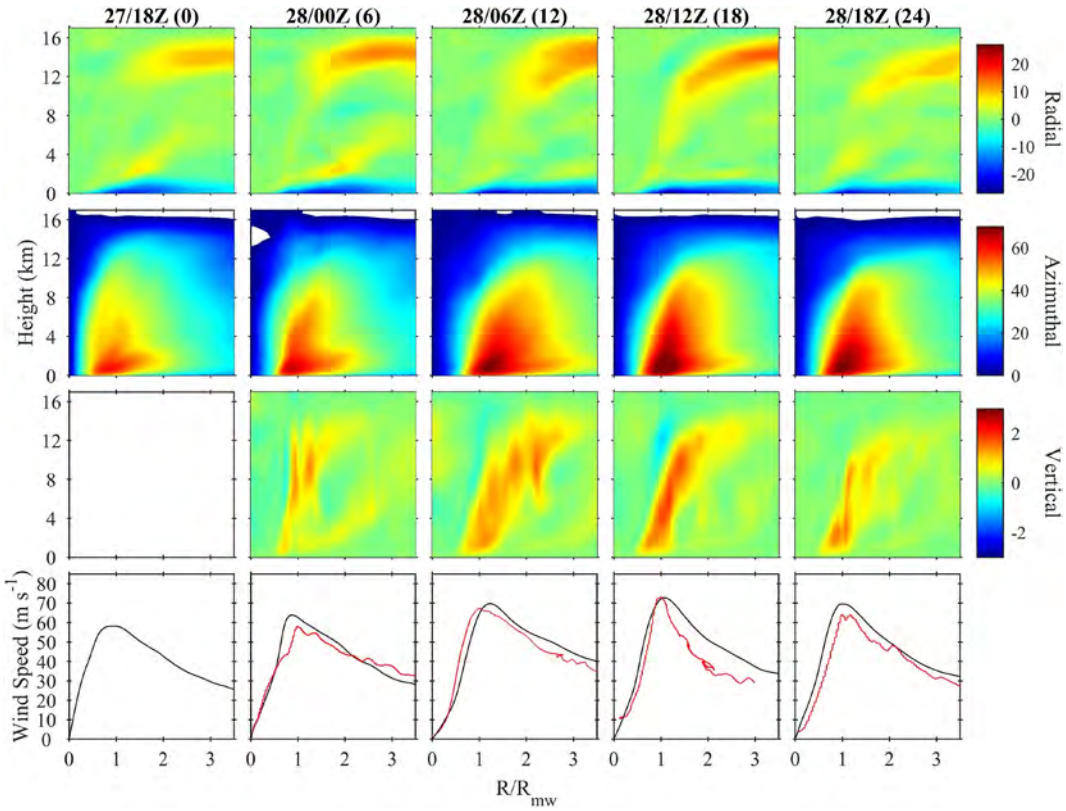

Figure 4. (Top three panels) The azimuthally averaged radial (top), azimuthal (middle), and vertical (bottom) wind components (m s^{-1}). (Bottom panel) Snapshots of the azimuthally averaged azimuthal wind (m s^{-1}) at 850-mb (black) compared to aircraft reconnaissance wind observations (red).

this, we see that the latent heat flux in the observed storm is approximately 25%–100% larger in the actual storm environment.

A similar comparison can be made for the temperatures and therefore the sensible heat flux. Using the SST and air temperature, at C10, ΔT is between 1 and 1.75 times larger in the observations than in the model; at C12, ΔT is between 1 and 2 times larger; at C13, ΔT is between 1.25 and 3 times larger; and at C22, ΔT is between 1.5 and 2 times larger. As a result, the sensible heat flux would also be much larger in the observations than in the HWRF simulation of Ian. We will link these findings about latent and sensible heat to the MSE budget in the discussion.

4.2. Thermodynamics

Following X. Chen et al. (2019) and Sobel et al. (2014), the vertically integrated MSE budget is defined as

$$\left\langle \frac{\partial k}{\partial t} \right\rangle = -\langle \boldsymbol{u} \cdot \nabla_p k \rangle - \left\langle \omega \frac{\partial h}{\partial p} \right\rangle + Q_{AS} + Q_{\mathrm{Rad}} \tag{14}$$

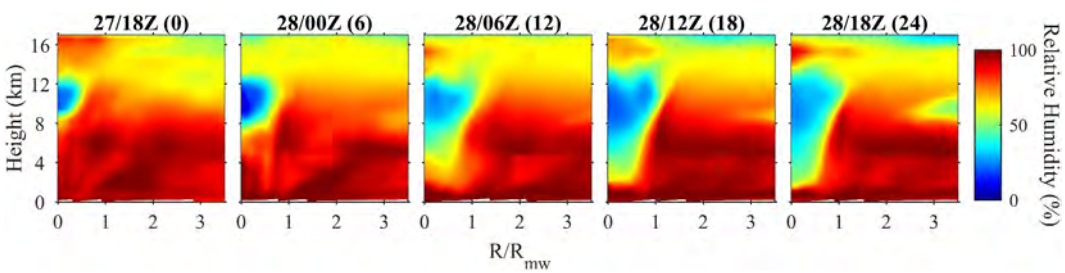

Figure 5. The azimuthally averaged relative humidity.

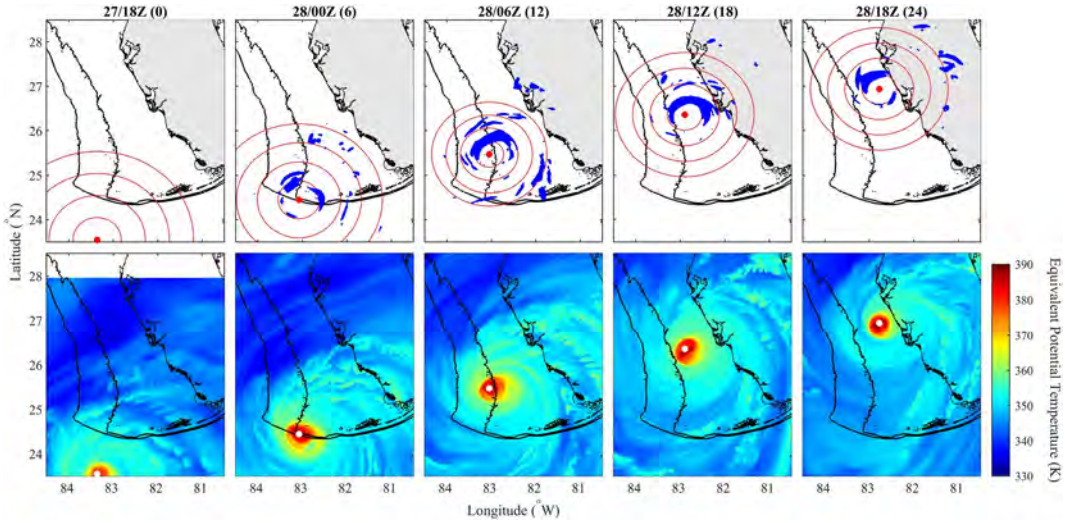

Figure 6. (top) The distribution of cloudbursts. The red dot represents the storm center in the Hurricane Weather Research Forecasting (HWRF) simulation, and the red square represents the storm center from the NOAA best track. The red circles outward from the center represent 1, 2, 3, and 4 times the radius of maximum wind. (bottom) The equivalent potential temperature relative to 1,000-mb (K). The white dot represents the storm center in the HWRF simulation.

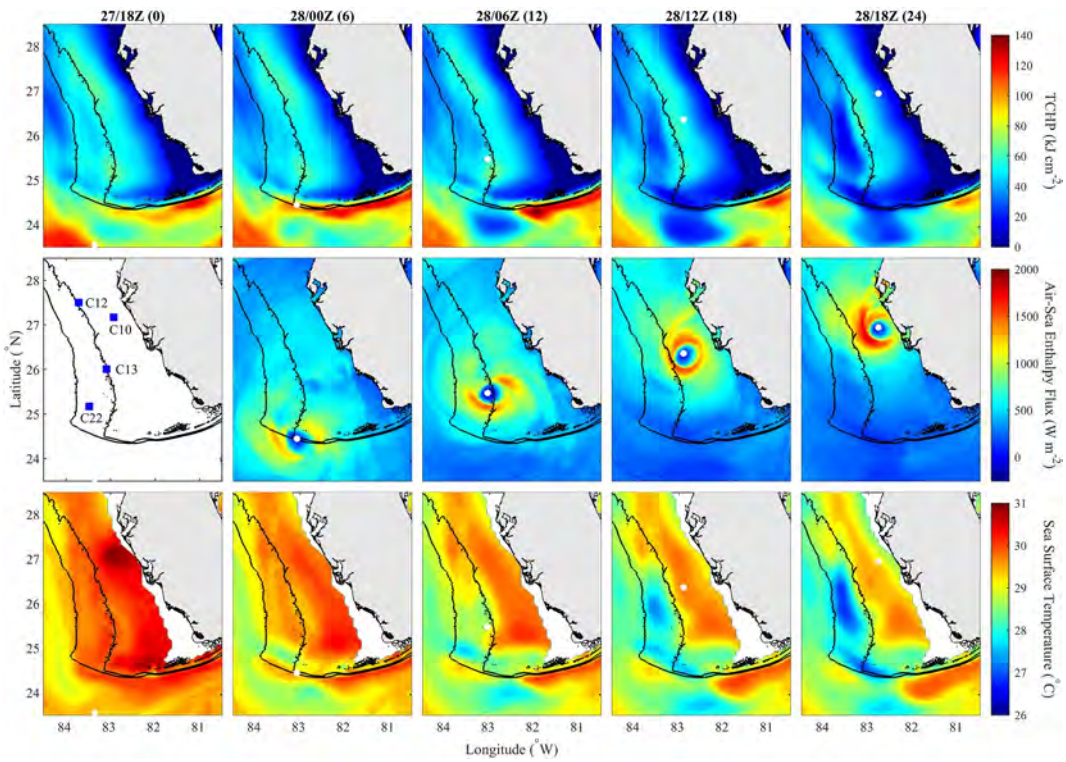

Figure 7. (top) The tropical cyclone heat potential (kJ cm^{-2}). (middle) The air-sea enthalpy flux (W m^{-2}). (bottom) The sea surface temperature (°C). The white dot represents the Hurricane Weather Research Forecasting-simulated storm center. The blue dots in the middle left panel show the locations of the four COMPS surface stations.

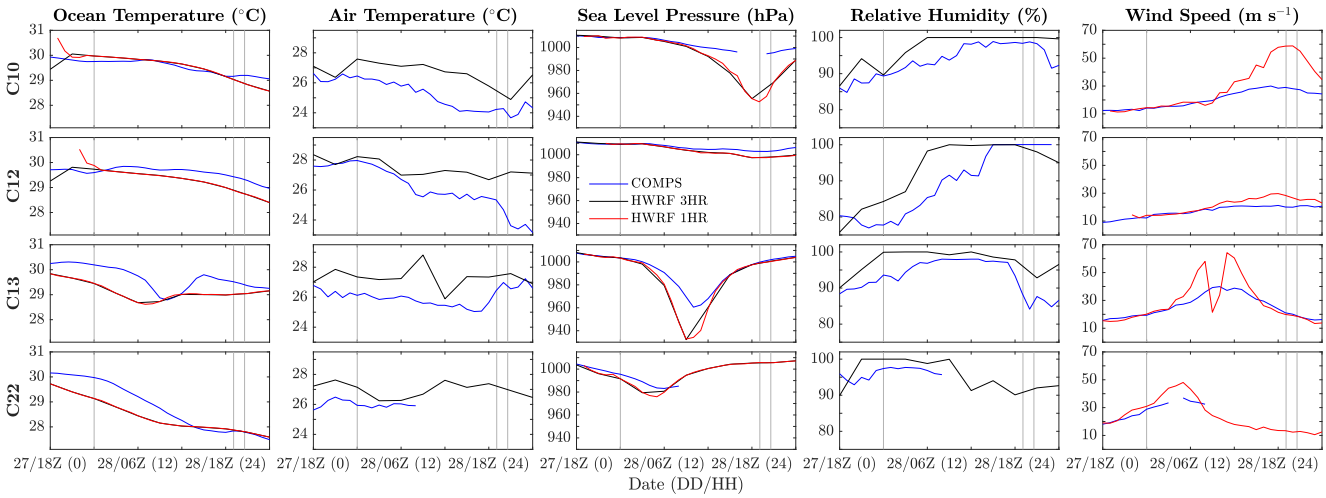

Figure 8. Sea surface temperatures, air temperatures, sea level pressure, relative humidity, and surface wind speeds from the four COMPS surface stations (blue) on the West Florida Shelf along with the Hurricane Weather Research Forecasting/POM interpolated values from the 3-hr (black) and 1-hr (red, where there are values from the 1-hr output). The vertical lines are as in Figure 1.

where the angle brackets represent the column-integrated quantity from the surface to the 100-hPa pressure level that is spatially averaged within 200 km of the storm center, $\boldsymbol{u}$ is the horizontal wind vector, $\nabla_p k$ is the gradient of the moist enthalpy at constant pressure, ω is the vertical wind speed, p is the pressure, Q_{AS} is the air-sea enthalpy flux, and Q_{Rad} is the sum of incoming and outgoing longwave and shortwave radiation terms, and the rest of the variables follow their standard definitions. This form of the equation, with k in place of h in the local and horizontal advection terms, gives better closure to the scheme (Neelin, 2007).

MSE is preferable over CAPE, which is not conserved, and regular static energy, which does not include a moisture term. As shown by X. Chen et al. (2019), MSE can be a useful indicator of RI in hurricanes as it is usually conserved (and transferred) or slightly increasing during such events.

The column-integrated MSE was fairly consistent over the time of RI, changing only in slight increments (Figure 9a). Throughout the RI period, the components of the MSE (Figure 9b) varied differently: the enthalpy term initially decreased and then increased, the geopotential term remained fairly constant, and the latent heat term consistently decreased until the end of RI. Advection contributed negatively to the MSE (Figure 9e), with the vertical term dominating the outflow of MSE (as in Fischer et al., 2023). In contrast, the air-sea enthalpy flux (mostly latent heat) and radiation terms remained fairly constant and positive during RI, with the radiation being much smaller than the flux (Figure 9d). Hence, the source and advection terms (Figure 9e) balance each other, with the local change term and the sum of the right hand side terms being approximately equal during RI, showing the model achieved approximate closure.

The azimuthally averaged DH rates in Ian were above 50 K hr^{-1} inside the radius of maximum wind, sloping along the updraft region of the eyewall (Figure 10), with pronounced cooling only found in the interior downdraft. Kuo et al. (2019, Figure 11) found DH rates of 3–14 K hr^{-1} during a period of much greater intensification (31 m s^{-1} in 24 hr), starting from a tropical storm. Kilroy et al. (2016), at 6 km above the surface, found DH rates greater than 25 K hr^{-1} in a storm that was weakening after RI. In Hurricane Patricia (2015), Martinez et al. (2019), using expendable dropsondes, found DH rates in excess of 200 K hr^{-1} in the eye of the storm during RI.

Azimuthal means of DH are more indicative of RI than the spatial distribution of DH (Montgomery et al., 2006; Nolan et al., 2007). Our findings agree with Vigh and Schubert's (2009) observation that the DH rate increases downdraft intensity inside the region of heating. In the convective ring model of storm intensification, DH induces radial inflow, leading to contraction of the eyewall and subsequent spin-up, which causes subsidence that leads to adiabatic heating and a pressure drop. This pressure drop maintains the gradient wind balance (e.g., Pendergrass & Willoughby, 2009; Willoughby, 1990; Willoughby et al., 1982).

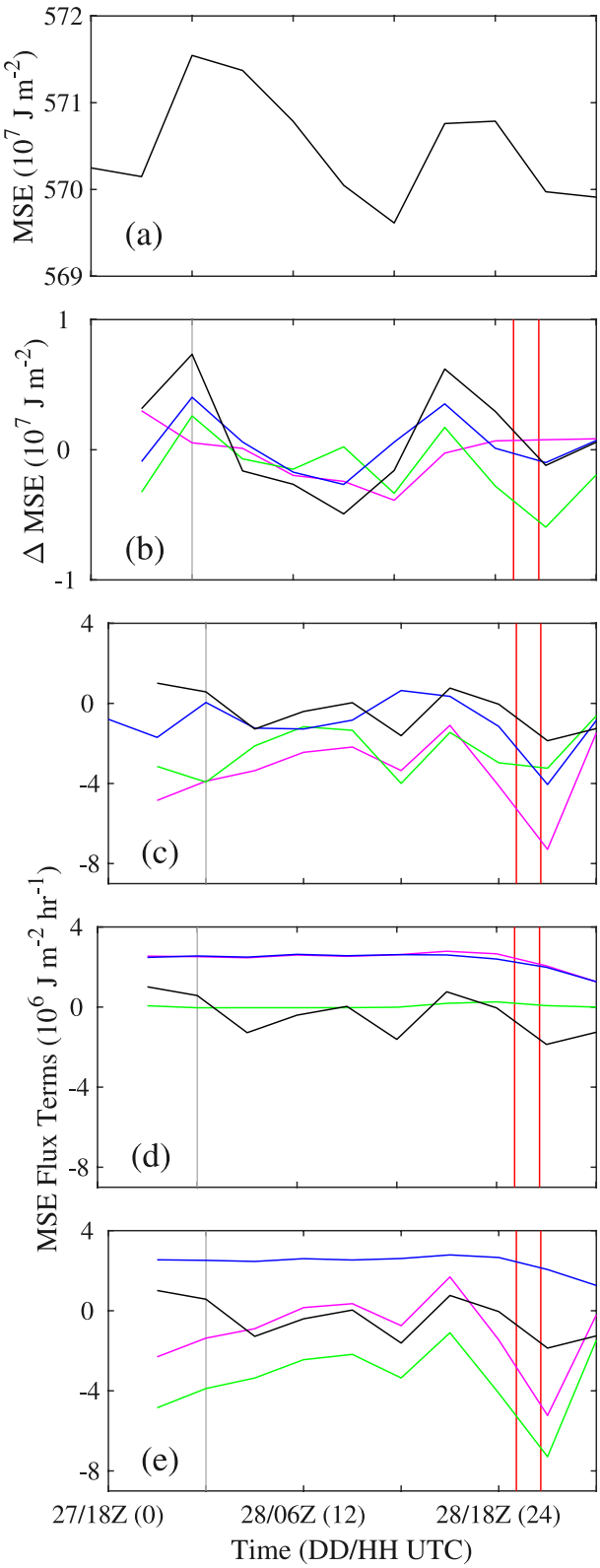

Figure 9.

Convection was concentrated within the core of the storm, which corresponds to the dominant process of latent heating that is strongest in the eyewall. In an unstable atmosphere ($\partial\theta_e/\partial p < 0$, which is not shown but is discussed later as it does apply to Ian), convection is further favored and initially manifests as outflow at the top of the storm (Figure 4), enhancing the secondary, or overturning, circulation (e.g., Bui et al., 2009; Carrier, 1971; Charney & Eliassen, 1964; Ooyama, 1969, 1982) with a radial outflow at the top of the storm and a radial inflow at the base of the storm. In an RI scenario (e.g., D.-L. Zhang et al., 2001), strong AAM advection is supergradient (e.g., Smith, 1968) at both the surface (inward) and at the top of the storm (outward). The radial wind in Ian showed an intensification in the inflow (outflow) at the base (top) of the storm in agreement with these theories.

4.3. Dynamics

The results of the AAM balance following Equation 8 are shown in Figure 11 in which the local derivative, advection, and eddy terms are shown along with the sum of the advection and eddy terms and the model residual. The limitations in the method are apparent from the residual, especially in the planetary boundary layer and in the eyewall, where residual values were an order of magnitude larger than the local tendency. A decrease in the AAM occurred in the outer regions of the storm and was accompanied by an increase in the eyewall and eye of the storm, indicating a net inward advection of AAM. The eddy and advection terms were nearly opposite of each other; in the lower portion of the eyewall, both terms were dominated by their radial component with the vertical advection dominating at the top of the eyewall due to venting aloft. These findings match those of J. A. Zhang and Rogers (2019) for Hurricane Earl (2010), which also underwent RI under moderate shear.

Intensification via AAM advection assumes that the total AAM is conserved within the storm and advected from one region to another. However, this assumption does not hold in the HWRF representation of Ian, where a large model residual was noted in the boundary layer and the eyewall during the peak of intensification. Intensification via azimuthal wind advection (e.g., Montgomery et al., 2014; Persing et al., 2013; Smith et al., 2017) should balance in the planetary boundary layer. Numerous studies (Montgomery & Persing, 2021; Montgomery et al., 2020; Persing et al., 2013; Smith et al., 2009, 2017) addressed such boundary layer issues. As seen in Figure 12, the agradient wind (note the difference in the colorbars) is above 10 m s^{-1} in the boundary layer, with the maximum of the agradient wind aligned with the AAM maximum, including a negative component along the spin down region of the eyewall (e.g., Eliassen, 1971; Eliassen & Lystad, 1977; Greenspan & Howard, 1963; Montgomery et al., 2001; Smith & Montgomery, 2015; Smith et al., 2017). The deepening of the azimuthal wind is much like that shown in DesRosiers et al. (2023) and DesRosiers and Bell (2024). Hence, we look at

Figure 9. (a) The moist static energy (MSE) (black line, MSE). (b) The time rate of change of the enthalpy (black), the geopotential (blue), the latent heat (green), and the latent heat of a saturated atmosphere (red). (c) Time rate of change of the moist enthalpy (black), the horizontal advection of moist enthalpy (blue), the vertical advection of enthalpy (green), and the total advection (magenta). (d) Time rate of change of the moist enthalpy (black), the air-sea enthalpy flux (blue), the total radiative flux (green), and the sum of the radiative and air-sea enthalpy fluxes (magenta). (e) The local change in MSE (black), the advection of MSE (green), the sources and sinks (blue), and the sum of all the right hand side terms of Equation 14 (magenta). The gray and red lines are as in Figure 1.

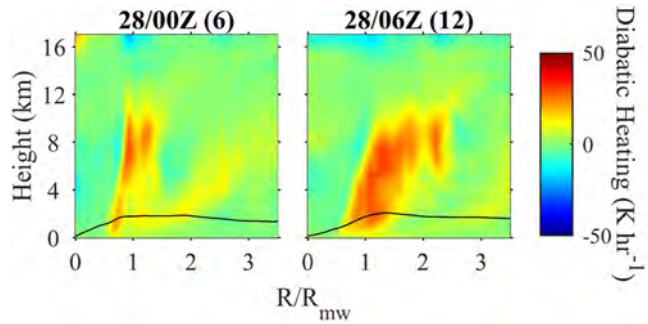

Figure 10. The diabatic heating, in K hr^{-1}. In all the panels, the black line represents the top of the planetary boundary layer as determined by Hurricane Weather Research Forecasting.

the azimuthal momentum budget (Figure 13) and indeed see a negative inflow in the planetary boundary layer, as was observed in the AAM budget.

5. Conclusions

Hurricane Ian (2022) was analyzed using a comprehensive combination of techniques that had previously been applied individually in the analysis of hurricanes but not all together in a single study. As Ian approached the southwest coast of Florida, the HWRF model accurately predicted the timing of the intensification of the storm while remaining within the margin of error for the track of the storm. Dynamic and thermodynamic analyses are combined with atmospheric and oceanographic parameters to explain Ian's RI on the WFS. Ian underwent two separate RIs, with the second RI occurring while it was already a major hurricane, resulting in it becoming a Category 5 storm characterized by the most intense winds and convection being found in the left front quadrant.

Similarities exist between Hurricane Ian and other hurricanes. Ian, much like Hurricane Dorian (2019), underwent RI in adverse conditions, with RI preceded by an increase in convection. Alvey et al. (2022) showed this using reconnaissance data, whereas we show this via cloudbursts in the HWRF simulation. Dorian, however, had much larger tilt (∼50 km between 2 and 6 km). Both Ian and Dorian had tilts within the 100-km threshold that Schecter and Menelaou (2020) showed to be essential rapid vortex realignment. The modeled track bias being downshear to the left of both the tilt and the shear and being too far downshear is consistent with the findings of Alvey et al. (2020, 2025). We include the caveat that we were looking at HWRF, whereas Alvey et al. (2025) and other recent studies have used the newer Hurricane Analysis and Forecast System (HAFS).

The latent heat remained large throughout the model run, with the TCHP being at or above the threshold for RI (>60 kJ cm^{-2}). This sustained heating balanced the loss of MSE due to advection, allowing the atmosphere to remain unstable, and contributed to the DH of the inner core region of the storm. The observed sea temperatures remained higher than those predicted in the POM/HWRF simulation. Assuming all other variables remained constant, then the latent heat flux would have been larger, likely leading to stronger and faster RI than predicted by the HWRF simulation. We show the observed air temperatures are lower than the HWRF values, the observed SSTs are higher, and the observed relative humidity is lower. In the HWRF simulation, latent heat offset the advective losses due to shear while providing enough heat to the atmosphere that RI took place despite the adverse conditions. In the actual storm, the latent and sensible heat fluxes may have been large enough to not only offset the advective loss of MSE but also possibly to increase the column-integrated MSE in Ian (e.g., Schecter, 2022).

The DH operated in a storm spin-up akin to that described in D.-L. Zhang et al. (2001) and Ooyama (1982), with the heating leading to an increase in both storm inflow and outflow (e.g., AAM and azimuthal momentum advection). The AAM and azimuthal momentum budgets are both in approximate balance, meaning that general conclusions can be made from these. Large contributions from the advective terms are balanced in the eyewall by the eddy terms. Strong convection and outflow, to conserve mass, cause a strong inflow of momentum that crosses the radius of maximum wind, leading to intensification (Smith et al., 2017). This process occurring in Ian, a storm with relatively low tilt, agrees with the findings of Fischer et al. (2024). Given the high sea temperatures on the WFS, further intensification likely would have occurred had the storm not made landfall over southwestern Florida.

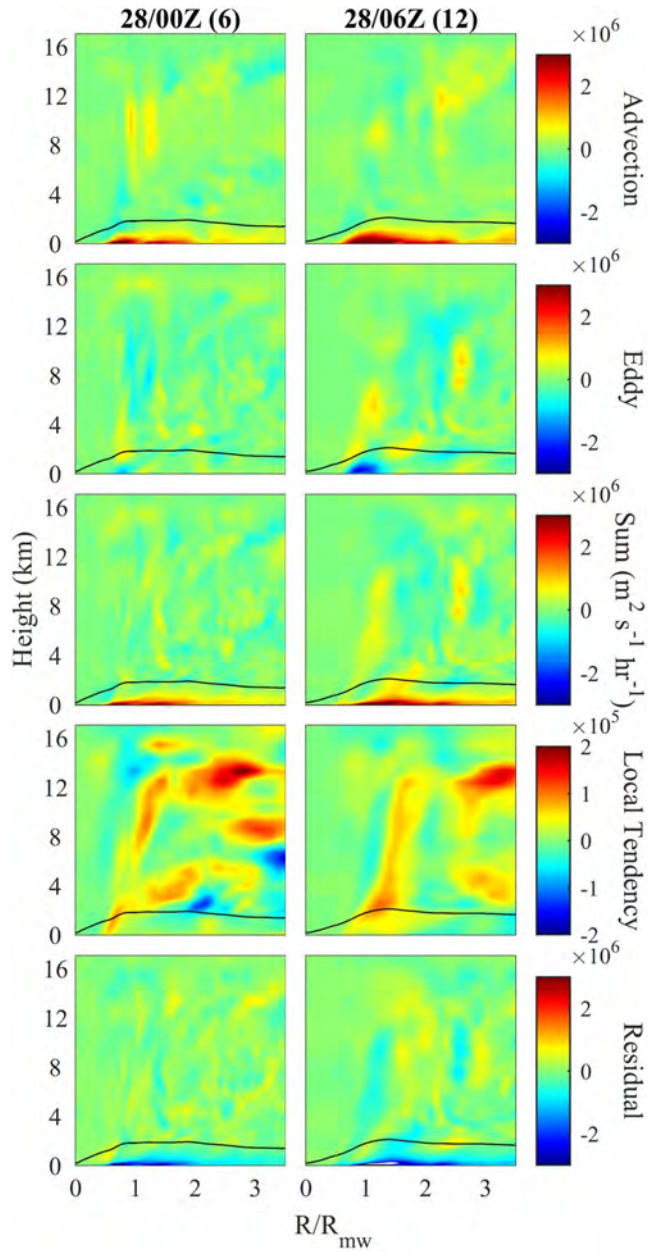

Figure 11. The absolute angular momentum budget. (top) The total advection. (second from top) The eddy terms. (middle) Sum of the advection and eddy terms. (second from bottom) The local change. (bottom) The model residual. In all the panels, the black line represents the top of the planetary boundary layer, and the units are $m^2\ s^{-1}\ hr^{-1}$. Note the different scales for the local tendency term.

Based on the above analyses, Hurricane Ian followed the classical RI paradigm that was succinctly summarized by D.-L. Zhang et al. (2001). High latent heat fluxes from the surface caused a net positive DH in the storm core. This heating is sufficient to offset advective losses at the top of the storm, leading to large DH in the storm core and driving a radial advection of boundary layer momentum that, upon deceleration, was lifted vertically, spinning up the storm. This process continued while Ian was over the anomalously warm shallow waters of the WFS. The storm continues to intensify until frictional effects from the Florida Peninsula begin to affect the storm. Even after this RI cycle, the WFS maintains a sufficient TCHP and SST to support further development. The decreasing effect of MSE advection shows an increasingly organized storm core that was heavily influenced by landfall. Hence, Ian was a storm that was still intensifying when frictional effects (possibly the loss of latent

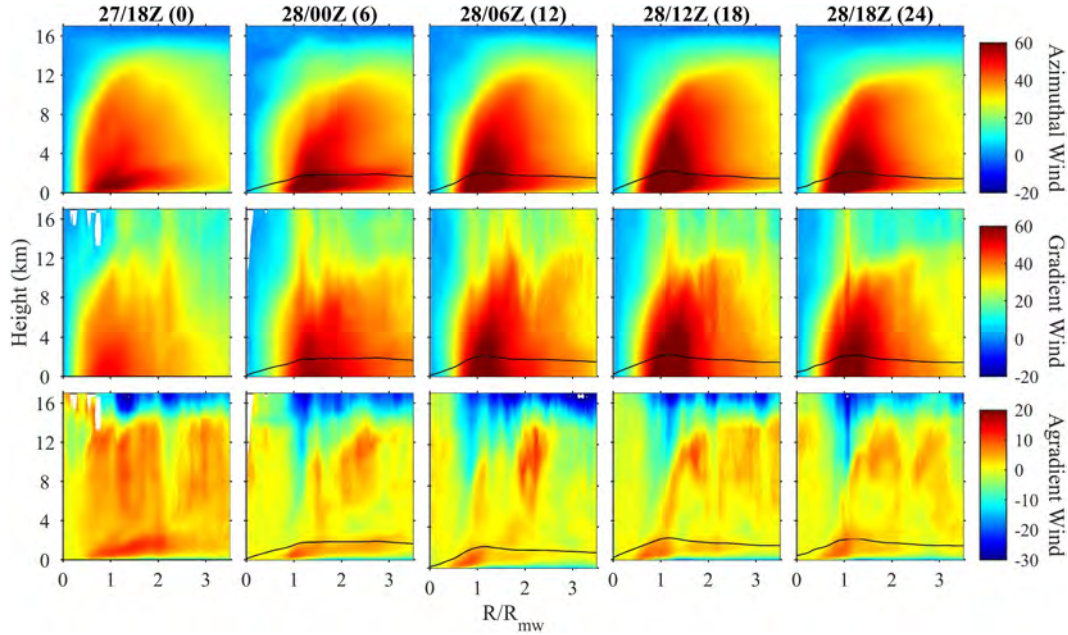

Figure 12. The azimuthally averaged azimuthal (top), gradient (middle), and agradient (bottom) wind components. In all the panels, the black line represents the top of the planetary boundary layer, and the units are m s^{-1}. Note the different scale for the agradient wind.

heating from the sea surface) became so great that the storm could no longer intensify. The roles of DH and asymmetric convection in driving vortex realignment and RI are similar to Feng et al.'s (2024) simulation of Super Typhoon Rammasun (2014).

Hurricane Ian underwent RI in a hybrid of the sprint and marathon modes, described by Judt et al. (2023) as a "fast marathon." Likewise, there are similarities to the "Type A" mode of Schecter (2024) for intensification beginning while the vortex is still misaligned, but Ian's main convection region was in the uptilt direction, not downtilt. Classification is difficult because the temporal resolution resolves the smaller timescale variations that characterize the modes. We state this because Ian's RI (a) suddenly occurred in (b) a high shear environment that had caused (c) a moderate tilt as in the sprint mode before (d) reorganizing as part of the RI. Throughout the simulation, Ian maintained a classic modified-Rankine vortex model (which can be approximately seen in Figure 4) as in the marathon mode and underwent a quasi-constant intensification rate over a 12-hr period. Unique to Ian was its original intensity at the time of RI initiation, but most of the environmental features that we observe in Ian are consistent with the findings of the recent literature with regard to RI for storms over deeper water.

Hurricane Ian's azimuthal wind budgets show some signatures that we could not explain using the standard methods. In this study as well as in the previous studies, one value of the radius of maximum wind (that from 850 hPa) was used at all levels of the storm. Would using the unique radius of maximum wind from each model level lead to more exact results? Further analyses are needed to explain why the left front quadrant became the strongest quadrant instead of the right front, something that is seen in both the HWRF simulation and in observations. These results show that improvements in atmospheric physics must be accompanied by improvements in the coupled ocean model as well.

In their analysis of Hurricane Sandy (2012), S. Li and Chen (2022) coupled the Finite Volume Community Ocean Model (FVCOM) to the WRF. They found that the FVCOM coupled model more accurately simulated Sandy's approach to the New Jersey coastline than the uncoupled model largely due to improved latent heat fluxes. We speculate that a higher resolution ocean model that more closely captured the actual ocean temperature structure on the WFS being coupled to HWRF could have resulted in a more accurate forecast intensity and track. As of the time of this writing, the new Hurricane Analysis and Forecast System (HAFS), which is coupled to the Hybrid Coordinate Ocean Model (HyCOM), has yet to encounter such a case of RI on the WFS. HyCOM, with a similar

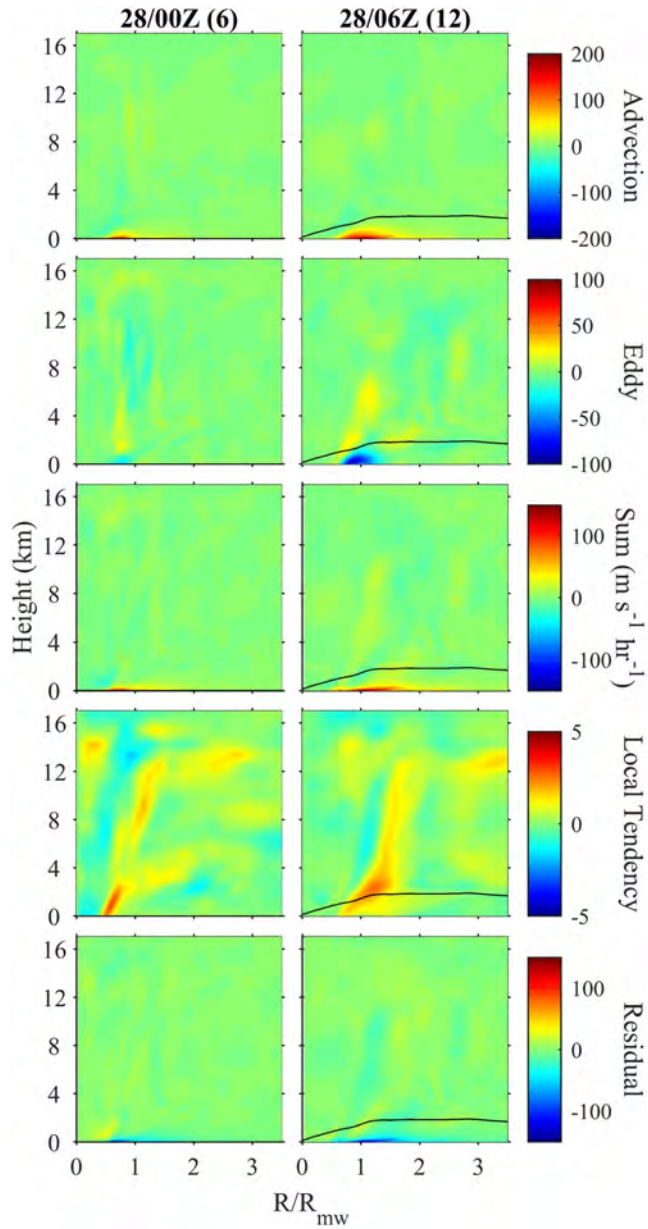

Figure 13. The azimuthal momentum budget. (top) The total advection. (second from top) The eddy terms. (middle) Sum of the advection and eddy terms. (second from bottom) The local change. (bottom) The model residual. In all the panels, the black line represents the top of the planetary boundary layer, and the units are m s^{-1} hr^{-1}. Note the variability in the colorbar scales.

resolution as POM (9 km), may be subject to the same coastal ocean temperature structure deficiency as observed with Ian. This highlights the importance of having actual water column temperature observations in the coastal ocean region subject to hurricane landfall and the consideration of using even higher resolution coastal ocean models coupled with atmospheric models for improved hurricane intensity and track forecasts.

Conflict of Interest

The authors declare no conflicts of interest relevant to this study.

Data Availability Statement

The in situ data from the West Florida Continental Shelf are available through the COMPS website at https://comps.marine.usf.edu:81/.

Acknowledgments
We would like to thank J. Law for the seagoing operations that maintain the COMPS stations from which the in situ temperature data were obtained. We thank Dennis Mayer, Kaili Qiao, and Jeff Donovan for in situ data quality control. Funding for this study was provided by NOAA/IOOS through the Southeast Coastal Ocean Observing Regional Association (SECOORA, award NA21NOS0120097), a cooperative agreement between NOAA's Office of Coast Survey and the University of South Florida through the Center for Ocean Mapping and Innovative Technologies (COMIT, award NA20NOS4000227), and Florida Flood Hub for Applied Research and Innovation. A.K. Nickerson also benefited from a graduate student fellowship (the Sanibel-Captiva Shell Club/Mary and Al Bridell Memorial Fellowship). Jun Zhang acknowledges support from U.S. National Science Foundation Awards 2228299 and 2211308 and National Oceanic and Atmospheric Administration Grants NA22OAR4590174, NA22OAR4590178, and NA22OAR4050669D. We thank Pallav Ray for his helpful comments that improved this manuscript. We also thank the three anonymous reviewers for their comments that helped improve this manuscript.

References

Aberson, S. D., & Kaplan, J. (2020). The relationship between the Madden-Julian Oscillation and tropical cyclone rapid intensification. *Weather and Forecasting*, *35*(5), 1865–1870. https://doi.org/10.1175/WAF-D-19-0209.1

Alvey, G. R., & Hazelton, A. (2022). How do weak, misaligned tropical cyclones evolve toward alignment? A multi-case study using the hurricane analysis and forecast system. *Journal of Geophysical Research: Atmospheres*, *127*(20), e2022JD037268. https://doi.org/10.1029/2022JD037268

Alvey, G. R., Alaka, G. J., Gramer, L., & Hazelton, A. (2025). Evaluation of Hurricane Analysis and Forecast System (HAFS) error statistics stratified by internal structure and environmental metrics. *Weather and Forecasting*, *40*, https://doi.org/10.1175/WAF-D-24-0030.1

Alvey, G. R., Fischer, M., Reasor, P., Zawislak, J., & Rogers, R. F. (2022). Observed processes underlying the favorable vortex repositioning early in the development of Hurricane Dorian (2019). *Monthly Weather Review*, *150*(1), 193–213. https://doi.org/10.1175/MWR-D-21-0069.1

Alvey, G. R., Zipser, E., & Zawislak, J. (2020). How does Hurricane Edouard (2014) evolve toward symmetry before rapid intensification? A high-resolution ensemble study. *Journal of the Atmospheric Sciences*, *77*(4), 1329–1351. https://doi.org/10.1175/JAS-D-18-0355.1

Balaguru, K., Foltz, G. R., Leung, L. R., Kaplan, J., Xu, W., Reul, N., & Chapron, B. (2020). Pronounced impact of salinity on rapidly intensifying tropical cyclones. *Bulletin of the American Meteorological Society*, *101*(9), E1497–E1511. https://doi.org/10.1175/BAMS-D-19-0303.1

Bhatia, K., Baker, A., Yang, W., Vecchi, G., Knutson, T., Murakami, H., et al. (2022). A potential explanation for the global increase in tropical cyclone rapid intensification. *Nature Communications*, *13*(1), 6626. https://doi.org/10.1038/s41467-022-34321-6

Biswas, M. K., Abarca, S., Bernardet, L., Ginis, I., Grell, E., Iacono, M., et al. (2018). Hurricane Weather research and forecasting (HWRF) model: 2018 Scientific documentation (p. 112).

Biswas, M. K., Carson, L., Newman, K., Stark, D., Kalina, E., Grell, E., & Frimel, J. (2018). Community HWRF Users' Guide V4.0a (p. 162).

Bolton, D. B. (1980). The computation of equivalent potential temperature. *Monthly Weather Review*, *108*(7), 1046–1053. https://doi.org/10.1175/1520-0493(1980)108<1046:TCOEPT>2.0.CO;2

Bosart, L. F., Bracken, W. E., Molinari, J., Velden, C. S., & Black, P. G. (2000). Environmental influences on the rapid intensification of Hurricane Opal (1995) over the Gulf of Mexico. *Monthly Weather Review*, *128*(2), 322–352. https://doi.org/10.1175/1520-0493(2000)128<0322:EIOTRI>2.0.CO;2

Bui, H. H., Smith, R. K., Montgomery, M. T., & Peng, J. (2009). Balanced and unbalanced aspects of tropical-cyclone intensification. *Quarterly Journal of the Royal Meteorological Society*, *135*(644), 1715–1731. https://doi.org/10.1002/qj.502

Carrier, G. F. (1971). Swirling flow boundary layers. *Journal of Fluid Mechanics*, *49*(1), 133–144. https://doi.org/10.1017/S0022112071001964

Carstens, J. D., Didlake, A. C., & Zarzycki, C. M. (2024). Tropical cyclone wind shear-relative asymmetry in reanalyses. *Journal of Climate*, *37*(22), 5793–5816. https://doi.org/10.1175/JCLI-D-23-0628.1

Charney, J. G., & Eliassen, A. (1964). On the growth of the hurricane depression. *Journal of the Atmospheric Sciences*, *21*(1), 68–75. https://doi.org/10.1175/1520-0469(1964)021%3C0068:OTGOTH%3E2.0.CO;2

Chen, H., & Gopalakrishnan, S. G. (2015). A study on the asymmetric rapid intensification of hurricane Earl (2010) using the HWRF system. *Journal of the Atmospheric Sciences*, *72*(2), 531–550. https://doi.org/10.1175/JAS-D-14-0097.1

Chen, H., Zhang, D.-L., Carton, J., & Atlas, R. (2011). On the rapid intensification of Hurricane Wilma (2005). Part I: Model prediction and structural changes. *Weather and Forecasting*, *26*(6), 885–901. https://doi.org/10.1175/WAF-D-11-00001.1

Chen, X., Wang, Y., Fang, J., & Xue, M. (2018). A numerical study on rapid intensification of Typhoon Vicente (2012) in the South China Sea. Part II: Roles of inner-core processes. *Journal of the Atmospheric Sciences*, *75*(1), 235–255. https://doi.org/10.1175/JAS-D-17-0129.1

Chen, X., Xue, M., & Fang, J. (2018). Rapid Intensification of Typhoon Mujigae (2015) under different sea surface temperatures: Structural changes leading to rapid intensification. *Journal of the Atmospheric Sciences*, *75*(12), 4313–4335. https://doi.org/10.1175/JAS-D-18-0017.1

Chen, X., Zhang, J. A., & Marks, F. D. (2019). A thermodynamic pathway leading to rapid intensification of tropical cyclones in shear. *Geophysical Research Letters*, *46*(15), 9241–9251. https://doi.org/10.1029/2019GL083667

DeMaria, M., & Kaplan, J. (1994). A statistical hurricane intensity prediction scheme (SHIPS) for the Atlantic basin. *Weather and Forecasting*, *9*(2), 209–220. https://doi.org/10.1175/1520-0434(1994)009%3C0209:ASHIPS%3E2.0.CO;2

DeMaria, M., Franklin, J. L., Zelinsky, R., Zelinsky, D. A., Onderline, M. J., Knaff, J. A., et al. (2022). The National Hurricane Center tropical cyclone model guidance suite. *Weather and Forecasting*, *37*(11), 2141–2159. https://doi.org/10.1175/WAF-D-22-0039.1

DeMaria, M., Mainelli, M., Shay, L. K., Knaff, J. A., & Kaplan, J. (2005). Further improvements to the statistical hurricane intensity prediction scheme (SHIPS). *Weather and Forecasting*, *20*(4), 531–543. https://doi.org/10.1175/WAF862.1

DesRosiers, A. J., & Bell, M. M. (2024). Dynamic vortex height evolution during tropical cyclone rapid intensification. *Journal of Geophysical Research: Atmospheres*, *129*(24), e2024JD041710. https://doi.org/10.1029/2024JD041710

DesRosiers, A. J., Bell, M. M., & Cha, T.-Y. (2022). Vertical vortex development in Hurricane Michael (2018) during rapid intensification. *Monthly Weather Review*, *150*(1), 99–114. https://doi.org/10.1175/MWR-D-21-0098.1

DesRosiers, A. J., Bell, M. M., Klotzbach, P. J., Fischer, M. S., & Reasor, P. D. (2023). Observed relationships between tropical cyclone vortex height, intensity, and intensification rate. *Geophysical Research Letters*, *50*(8), e2022GL101877. https://doi.org/10.1029/2022GL101877

Dunion, J. P., Thorncroft, C. D., & Nolan, D. S. (2019). Tropical cyclone diurnal cycle Signals in a hurricane Nature run. *Monthly Weather Review*, *147*(1), 363–388. https://doi.org/10.1175/MWR-D-18-0130.1

Eliassen, A. (1971). On the Ekman layer in a circular vortex. *Journal of the Meteorological Society of Japan*, *49*, 784–789. https://doi.org/10.2151/jmsj1965.49A.0_784

Eliassen, A., & Lystad, M. (1977). The Ekman layer of a circular vortex: A numerical and theoretical study. *Geophysica Norvegica*, *31*, 1–16.

Emanuel, K. (2018). 100 years of progress in tropical cyclone research. *Meteorological Monographs*, *59*, 15.1–15.68. https://doi.org/10.1175/AMSMONOGRAPHS-D-18-0016.1

Feng, Y., Wu, L., Zhou, X., & Xie, T. (2024). Vortex alignment during the rapid intensification of the simulated Typhoon Rammasun (2014) in moderate vertical shear. *Atmospheric Research*, *305*, 107415. https://doi.org/10.1016/j.atmosres.2024.107415

Fischer, M. S., Reasor, P. D., Rogers, R. F., & Gamache, J. F. (2022). An analysis of tropical cyclone vortex and convective characteristics in relation to storm intensity using a novel airborne Doppler Radar database. *Monthly Weather Review*, *150*(9), 2255–2278. https://doi.org/10.1175/MWR-D-21-0223.1

Fischer, M. S., Reasor, P. D., Tang, B. H., Corbosiero, K. L., Torn, R. D., & Chen, X. (2023). A tale of two vortex evolutions: Using a high-resolution ensemble to assess the impacts of ventilation on a tropical cyclone rapid intensification event. *Monthyly Weather Review*, *151*(1), 297–320. https://doi.org/10.1175/MWR-D-22-0037

Fischer, M. S., Rogers, R. F., Reasor, P. D., & Dunion, J. P. (2024). An observational analysis of the relationship between tropical cyclone vortex tilt, precipitation structure, and intensity change. *Monthly Weather Review*, *152*(1), 203–226. https://doi.org/10.1175/MWR-D-23-0089.1

Frank, W. M., & Ritchie, E. A. (2001). Effects of vertical wind shear on the intensity and structure of numerically simulated hurricanes. *Monthly Weather Review*, *129*(9), 2249–2269. https://doi.org/10.1175/1520-0493(2001)129<2249:EOVWSO>2.0.CO;2

Gao, Q., & Wang, Y. (2024). Dependence of tropical cyclone weakening rate in response to an imposed moderate environmental vertical wind shear on the warm-core strength and height of the initial vortex. *Geophysical Research Letters*, *51*(7), e2023GL107779. https://doi.org/10.1029/2023GL107779

Greenspan, H. P., & Howard, L. N. (1963). On a time-dependent motion of a rotating fluid. *Journal of Fluid Mechanics*, *17*(3), 385–404. https://doi.org/10.1017/S0022112063001415

Huang, Q., & Ge, X. (2023). Sensitivity of tropical cyclone development to the vortex size under vertical wind shear. *Journal of Geophysical Research: Atmospheres*, *128*(23), e2023JD038802. https://doi.org/10.1029/2023JD038802

Judt, F., Rios-Berrios, R., & Bryan, G. H. (2023). Marathon versus Sprint: Two modes of tropical cyclone rapid intensification in a global convection-permitting simulation. *Monthly Weather Review*, *151*(10), 2683–2699. https://doi.org/10.1175/MWR-D-23-0038.1

Juračič, A., & Raymond, D. J. (2016). The effects of moist entropy and moisture budgets on tropical cyclone development. *Journal of Geophysical Research: Atmospheres*, *121*(16), 9458–9473. https://doi.org/10.1002/2016JD025065

Kaplan, J., DeMaria, M., & Knaff, J. A. (2010). A revised tropical cyclone rapid intensification index for the Atlantic and eastern North Pacific basins. *Weather and Forecasting*, *25*(1), 220–241. https://doi.org/10.1175/2009WAF2222280.1

Kaplan, J., Rozoff, C. M., DeMaria, M., Sampson, C. R., Kossin, J. P., Velden, C. S., et al. (2015). Evaluating environmental impacts on tropical cyclone rapid intensification predictability utilizing statistical models. *Weather and Forecasting*, *30*(5), 1374–1396. https://doi.org/10.1175/WAF-D-15-0032.1

Kilroy, G., Smith, R. K., & Montgomery, M. T. (2016). Why do model tropical cyclones grow progressively in size and decay in intensity after reaching Maturity? *Journal of the Atmospheric Sciences*, *73*(2), 487–503. https://doi.org/10.1175/JAS-D-15-0157.1

Kim, S.-H., Lee, W., Kang, H.-W., & Kang, S. K. (2024). Predicting rapid intensification of tropical cyclones in the western north Pacific: A machine learning and net energy gain rate approach. *Frontiers in Marine Science*, *10*, 1296274. https://doi.org/10.3389/fmars.2023.1296274

Ko, M., Chen, X., Kubat, M., & Gopalakrishnan, S. (2023). The development of a Consensus machine learning model for hurricane rapid intensification forecasts with hurricane Weather research and forecasting (HWRF) data. *Weather and Forecasting*, *38*(8), 1253–1270. https://doi.org/10.1175/WAF-D-22-0217.1

Kuo, H.-C., Tsujino, S., Huang, C.-C., Wang, C.-C., & Tsuboki, K. (2019). Diagnosis of the dynamic efficiency of latent heat release and the rapid intensification of Supertyphoon Haiyan (2013). *Monthly Weather Review*, *147*(4), 1127–1147. https://doi.org/10.1175/MWR-D-18-0149.1

Leipper, D. F., & Volgenau, D. (1972). Hurricane heat potential of the Gulf of Mexico. *Journal of Physical Oceanography*, *2*(3), 218–224. https://doi.org/10.1175/1520-0485(1972)002<0218:HHPOTG>2.0.CO;2

Li, S., & Chen, C. (2022). Air-sea interaction processes during Hurricane Sandy: Coupled WRF–FVCOM model simulations. *Progress in Oceanography*, *206*, 102855. https://doi.org/10.1016/j.pocean.2022.102855

Li, Y., Wang, Y., Lin, Y., & Wang, X. (2021). Why does rapid contraction of the radius of maximum wind precede rapid intensification in tropical cyclones? *Journal of the Atmospheric Sciences*, *78*, 3441–3453. https://doi.org/10.1175/JAS-D-21-0129.1

Li, Z., & Weisberg, R. H. (1999a). West Florida continental shelf response to upwelling favorable wind forcing, 2: Dynamics. *Journal of Geophysical Research*, *104*(C10), 23427–23442. https://doi.org/10.1029/1999JC900205

Li, Z., & Weisberg, R. H. (1999b). West Florida shelf response to upwelling favorable wind forcing: Kinematics. *Journal of Geophysical Research*, *104*(C6), 13507–13527. https://doi.org/10.1029/1999JC900073

Liu, Y., Weisberg, R. H., Lenes, J. M., Zheng, L., Hubbard, K., & Walsh, J. J. (2016). Offshore forcing on the "pressure point" of the West Florida Shelf: Anomalous upwelling and its influence on harmful algal blooms. *Journal of Geophysical Research: Oceans*, *121*(8), 5501–5515. https://doi.org/10.1002/2016JC011938

Liu, Y., Weisberg, R. H., Sorinas, L., Law, J., & Nickerson, A. K. (2025). Rapid intensification of Hurricane Ian in relation to anomalously warm subsurface water on the wide continental shelf. *Geophysical Research Letters*, *52*(1), e2024GL113192. https://doi.org/10.1029/2024GL113192

Mainelli, M., DeMaria, M., Shay, L. K., & Goni, G. (2008). Application of oceanic heat content estimation to operational forecasting of recent Atlantic Category 5 hurricanes. *Weather and Forecasting*, *23*(1), 3–16. https://doi.org/10.1175/2007WAF2006111.1

Martinez, J., Bell, M. M., Rogers, R. F., & Doyle, J. D. (2019). Axisymmetric potential vorticity evolution of Hurricane Patricia (2015). *Journal of the Atmospheric Sciences*, *76*(7), 2043–2063. https://doi.org/10.1175/JAS-D-18-0373.1

Miyamoto, Y., & Nolan, D. S. (2018). Structural changes preceding rapid intensification in tropical cyclones as shown in a large ensemble of idealized simulations. *Journal of the Atmospheric Sciences*, *75*(2), 555–569. https://doi.org/10.1175/JAS-D-17-0177.1

Molinari, J., & Vollaro, D. (2010). Rapid intensification of a sheared tropical storm. *Monthly Weather Review*, *138*(10), 3869–3885. https://doi.org/10.1175/2010MWR3378.1

Montgomery, M. T., & Persing, J. (2021). Does balance dynamics well capture the secondary circulation and spinup of a simulated hurricane? *Journal of the Atmospheric Sciences*, *78*(1), 75–95. https://doi.org/10.1175/JAS-D-19-0258.1

Montgomery, M. T., Kilroy, G., Smith, R. K., & Črnivec, N. (2020). Contribution of mean and eddy momentum processes to tropical cyclone intensification. *Quarterly Journal of the Royal Meteorological Society*, *146*(732), 3101–3117. https://doi.org/10.1002/qj.3837

Montgomery, M. T., Nicholls, M. E., Cram, T. A., & Saunders, A. B. (2006). A vortical hot tower route to tropical cyclogenesis. *Journal of the Atmospheric Sciences*, *63*(1), 355–386. https://doi.org/10.1175/JAS3604.1

Montgomery, M. T., Snell, H. D., & Yang, Z. (2001). Axisymmetric spindown dynamics of hurricane-like vortices. *Journal of the Atmospheric Sciences*, *58*(5), 421–435. https://doi.org/10.1175/1520-0469(2001)058,0421:ASDOHL.2.0.CO;2

Montgomery, M. T., Zhang, J. A., & Smith, R. K. (2014). An analysis of the observed low-level structure of rapidly intensifying and mature Hurricane Earl (2010). *Quarterly Journal of the Royal Meteorological Society*, *140*(684), 2132–2146. https://doi.org/10.1002/qj.2283

Nam, C. C., Bell, M. M., & Tao, D. (2023). Bifurcation points for tropical cyclone genesis and intensification in sheared and dry environments. *Journal of the Atmospheric Sciences*, *80*(9), 2239–2259. https://doi.org/10.1175/JAS-D-22-0100.1

Nebylitsa, S., Majumdar, S. J., & Nolan, D. S. (2023). Revisiting environmental wind and moisture calculations in the context of tropical cyclone intensification. *Weather and Forecasting*, *38*(10), 2077–2094. https://doi.org/10.1175/WAF-D-23-0045.1

Neelin, J. D. (2007). Moist dynamics of tropical convection zones in monsoons, teleconnections and global warming. In T. Schneider & A. H. Sobel (Eds.), *The global circulation of the atmosphere* (pp. 267–301). Princeton University Press. https://doi.org/10.1515/9780691236919-012

Neelin, J. D., & Held, I. M. (1987). Modeling tropical convergence based on the moist static energy budget. *Monthly Weather Review*, *115*(1), 3–12. https://doi.org/10.1175/1520-0493(1987)115%3C0003:MTCBOT%3E2.0.CO;2

Nguyen, L. T., & Molinari, J. (2012). Rapid intensification of a sheared, fast-moving hurricane over the Gulf Stream. *Monthly Weather Review*, *140*(10), 3361–3378. https://doi.org/10.1175/MWR-D-11-00293.1

Nolan, D. S., & McGauley, M. G. (2012). In K. Oouchi & H. Fudeyasu (Eds.), *Tropical cyclogenesis in wind shear: Climatological relationships and physical processes. Cyclones: Formation, Triggers, and Control* (pp. 1–36). Nova Science Publishers.

Nolan, D. S., Moon, Y., & Stern, D. P. (2007). Tropical cyclone intensification from asymmetric convection: Energetics and efficiency. *Journal of the Atmospheric Sciences*, *64*(10), 3377–3405. https://doi.org/10.1175/JAS3988.1

Nolan, D. S., Nebylitsa, S., McNoldy, B. D., & Majumar, S. J. (2023). Modulation of tropical cyclone rapid intensification by mesoscale asymmetries. *Quarterly Journal of the Royal Meteorlogical Society*, *150*(758), 388–415. https://doi.org/10.1002/qj.4602

Ooyama, K. V. (1969). Numerical simulation of the life cycle of tropical cyclones. *Journal of the Atmospheric Sciences*, *26*(1), 3–40. https://doi.org/10.1175/1520-0469(1969)026%3C0003:NSOTLC%3E2.0.CO;2

Ooyama, K. V. (1982). Conceptual evolution of the theory and modeling of the tropical cyclone. *Journal of the Meteorological Society of Japan*, *60*(1), 369–380. https://doi.org/10.2151/jmsj1965.60.1_369

Pendergrass, A. G., & Willoughby, H. E. (2009). Diabatically induced secondary flows in tropical cyclones. Part I: Quasi-steady forcing. *Monthly Weather Review*, *137*(3), 805–821. https://doi.org/10.1175/2008MWR2657.1

Persing, J., Montgomery, M. T., McWilliams, J. C., & Smith, R. K. (2013). Asymmetric and axisymmetric dynamics of tropical cyclones. *Atmospheric Chemistry and Physics*, *13*(24), 12299–12341. https://doi.org/10.5194/acp-13-12299-2013

Potter, H., DiMarco, S. F., & Knap, A. H. (2019). Tropical cyclone heat potential and the rapid intensification of Hurricane Harvey in the Texas Bight. *Journal of Geophysical Research: Oceans*, *124*(4), 2440–2451. https://doi.org/10.1029/2018JC014776

Qin, N., Zhang, D.-L., & Li, Y. (2016). A statistical analysis of steady eyewall sizes associated with rapidly intensifying hurricanes. *Weather and Forecasting*, *31*(3), 737–742. https://doi.org/10.1175/WAF-D-16-0016.1

Reasor, P. D., & Eastin, M. D. (2012). Rapidly intensifying hurricane Guillermo (1997). Part II: Resilience in shear. *Monthly Weather Review*, *140*(2), 425–444. https://doi.org/10.1175/MWR-D-11-00080.1

Richardson, J. C., Torn, R. D., & Tang, B. H. (2022). An analog comparison between rapidly and slowly intensifying tropical cyclones. *Monthly Weather Review*, *150*(8), 2139–2156. https://doi.org/10.1175/MWR-D-21-0260.1

Rios-Berrios, R. (2020). Impacts of radiation and cold pools on the intensity and vortex tilt of weak tropical cyclones interacting with vertical wind shear. *Journal of the Atmospheric Sciences*, *77*(2), 669–689. https://doi.org/10.1175/JAS-D-19-0159.1

Rios-Berrios, R., Davis, C. A., & Torn, R. D. (2018). A hypothesis for the intensification of tropical cyclones under moderate vertical wind shear. *Journal of the Atmospheric Sciences*, *75*(12), 4149–4173. https://doi.org/10.1175/JAS-D-18-0070.1

Rios-Berrios, R., Finocchio, R. P. M., Alland, J. J., Chen, X., Fischer, M. S., Stevenson, S. N., & Tao, D. (2024). A review of the interactions between tropical cyclones and environmental vertical wind shear. *Journal of the Atmospheric Sciences*, *81*(4), 713–741. https://doi.org/10.1175/JAS-D-23-0022.1

Rogers, R. F., Reasor, P. D., & Zhang, J. A. (2015). Multiscale structure and evolution of Hurricane Earl (2010) during rapid intensification. *Monthly Weather Review*, *143*(2), 536–562. https://doi.org/10.1175/MWR-D-14-00175.1

Rogers, R. F., Reasor, P. D., Zawislak, J. A., & Nguyen, L. T. (2020). Precipitation processes and vortex alignment during the intensification of a weak tropical cyclone in moderate vertical shear. *Monthly Weather Review*, *148*(5), 1899–1929. https://doi.org/10.1175/MWR-D-19-0315.1

Rogers, R. F., Reasor, P., & Lorsolo, S. (2013). Airborne Doppler observations of the inner-core structural differences between intensifying and steady-state tropical cyclones. *Monthly Weather Review*, *141*(9), 2970–2991. https://doi.org/10.1175/MWR-D-12-00357.1

Rogers, R. F., Zhang, J. A., Zawislak, J., Jiang, H., Alvey, G., Zipser, E., & Stevenson, S. (2016). Observations of the structure and evolution of Hurricane Edouard (2014) during intensity change. Part II: Kinematic structure and the distribution of deep convection. *Monthly Weather Review*, *144*(9), 3355–3376. https://doi.org/10.1175/MWR-D-16-0017.1

Ryglicki, D. R., Cossuth, J. H., Hodyss, D., & Doyle, J. D. (2018). The unexpected rapid intensification of tropical cyclones in moderate vertical wind shear. Part I: Overview and observations. *Monthly Weather Review*, *146*(11), 3773–3800. https://doi.org/10.1175/MWR-D-18-0020.1

Ryglicki, D. R., Doyle, J. D., Hodyss, D., Cossuth, J. H., Jin, Y., Viner, K. C., & Schmidt, J. M. (2019). The unexpected rapid intensification of tropical cyclones in moderate vertical wind shear. Part III: Outflow–environment interaction. *Monthly Weather Review*, *147*(8), 2919–2940. https://doi.org/10.1175/MWR-D-18-0370.1

Ryglicki, D. R., Doyle, J. D., Jin, Y., Hodyss, D., & Cossuth, J. H. (2018). The unexpected rapid intensification of tropical cyclones in moderate vertical wind shear. Part II: Vortex tilt. *Monthly Weather Review*, *146*(11), 3801–3825. https://doi.org/10.1175/MWR-D-18-0021.1

Ryglicki, D. R., Velden, C. S., Reasor, P. D., Hodyss, D., & Doyle, J. D. (2021). Observations of Atypical rapid intensification characteristics in hurricane Dorian (2019). *Monthly Weather Review*, *149*, 2131–2150. https://doi.org/10.1175/MWR-D-20-0413.1

Salby, M. L. (1996). *Fundamentals of atmospheric physics*. Academic Press.627.

Schecter, D. A. (2022). Intensification of tilted tropical cyclones over relatively cool and warm oceans in idealized numerical simulations. *Journal of the Atmospheric Sciences*, *79*(2), 485–512. https://doi.org/10.1175/JAS-D-21-0051.1

Schecter, D. A. (2023). Intensification rates of tropical cyclone–like vortices in a model with downtilt diabatic forcing and oceanic surface drag. *Journal of the Atmospheric Sciences*, *80*(7), 1787–1813. https://doi.org/10.1175/JAS-D-22-0188.1

Schecter, D. A. (2024). Two types of transitions to relatively fast spinup in tropical cyclone simulations with weak-to-moderate environmental vertical wind shear. *Journal of the Atmospheric Science*, *81*(9), 1513–1541. https://doi.org/10.1175/JAS-D-23-0223.1

Schecter, D. A., & Menelaou, K. (2020). Development of a misaligned tropical cyclone. *Journal of the Atmospheric Sciences*, *77*(1), 79–111. https://doi.org/10.1175/JAS-D-19-0074.1

Shelton, K. L., & Molinari, J. (2009). Life of a six–hour hurricane. *Monthly Weather Review*, *137*(1), 51–67. https://doi.org/10.1175/2008MWR2472.1

Smith, R. K. (1968). The surface boundary layer of a hurricane. *Tellus*, *20*(3), 473–484. https://doi.org/10.1111/j.2153-3490.1968.tb00388.x

Smith, R. K., & Montgomery, M. T. (2015). Toward clarity on understanding tropical cyclone intensification. *Journal of the Atmospheric Sciences*, *72*(8), 3020–3031. https://doi.org/10.1175/JAS-D-15-0017.1

Smith, R. K., Montgomery, M. T., & Nguyen, S. V. (2009). Tropical cyclone spin-up revisited. *Quarterly Journal of the Royal Meteorological Society*, *135*(642), 1321–1335. https://doi.org/10.1002/qj.428

Smith, R. K., Zhang, J. A., & Montgomery, M. T. (2017). The dynamics of intensification in a hurricane Weather research and forecasting simulation of hurricane Earl (2010). *Quarterly Journal of the Royal Meteorological Society*, *143*(702), 293–308. https://doi.org/10.1002/qj.2922

Sobel, A., Wang, S., & Kim, D. (2014). Moist static energy budget of the MJO during DYNAMO. *Journal of the Atmospheric Sciences*, *71*(11), 4276–4291. https://doi.org/10.1175/JAS-D-14-0052.1

Sorinas, L., Weisberg, R. H., Liu, Y., & Law, J. (2023). Ocean-atmosphere heat exchange seasonal cycle on the West Florida Shelf derived from long term moored data. *Deep-Sea Research Part II*, *212*, 105341. https://doi.org/10.1016/j.dsr2.2023.105341

Stevenson, S., Corbosiero, K., & Molinari, J. (2014). The convective evolution and rapid intensification of Hurricane Earl (2010). *Monthly Weather Review*, *142*(11), 4364–4380. https://doi.org/10.1175/MWR-D-14-00078.1

Susca-Lopata, G., Zawislak, J., Zipser, E., & Rogers, R. (2015). The role of observed environmental conditions and precipitation evolution in the rapid intensification of Hurricane Earl (2010). *Monthly Weather Review*, *143*(6), 2207–2223. https://doi.org/10.1175/MWR-D-14-00283.1

Tang, X., & Zhang, F. (2016). Impacts of the diurnal radiation cycle on the formation, intensity, and structure of hurricane Edouard (2014). *Journal of the Atmospheric Sciences*, *73*(7), 2871–2892. https://doi.org/10.1175/JAS-D-15-0283.1

Vigh, J. L., & Schubert, W. H. (2009). Rapid development of the tropical cyclone warm core. *Journal of the Atmospheric Sciences*, *66*(11), 3335–3350. https://doi.org/10.1175/2009JAS3092.1

Wadler, J. B., Zhang, J. A., Jaimes, B., & Shay, L. K. (2018). Downdrafts and the evolution of boundary layer thermodynamics in Hurricane Earl (2010) before and during rapid intensification. *Monthly Weather Review*, *146*(11), 3545–3565. https://doi.org/10.1175/MWR-D-18-0090.1

Wallace, J. M., & Hobbs, P. V. (1977). *Atmospheric Science: An Introductory Survey*. Academic Press. https://doi.org/10.1016/C2009-0-00034-8 (p. 350).

Wang, C., Fang, J., & Ma, Y. (2022). Structural changes preceding the rapid intensification of Typhoon Lekima (2019) under moderate vertical wind shear. *Journal of Geophysical Research: Atmospheres*, *127*(20), e2022JD036544. https://doi.org/10.1029/2022JD036544

Weisberg, R. H., & He, R. (2003). Local and deep-ocean forcing contributions to anomalous water properties on the West Florida Shelf. *Journal of Geophysical Research*, *108*(C6), 15. https://doi.org/10.1029/2002JC001407

Weisberg, R. H., Barth, A., Alvera-Azcárate, A., & Zheng, L. (2009). A coordinated coastal ocean observing and modeling system for the West Florida Shelf. *Harmful Algae*, *8*, 585–598.

Weisberg, R. H., Li, Z., & Muller-Karger, F. E. (2001). West Florida shelf response to local wind forcing: April 1998. *Journal of Geophysical Research*, *106*, 31239–31262.

Weisberg, R. H., Zheng, L., & Liu, Y. (2015). Basic tenets for coastal ocean ecosystems monitoring. In Y. Liu, H. Kerkering, & R. H. Weisberg (Eds.), *Coastal Ocean observing systems*. Elsevier. https://doi.org/10.1016/B978-0-12-802022-7.00004-3

Whitaker, W. D. (1967). *Quantitative determination of heat transfer from sea to air during the passage of hurricane Betsy, M.S. Thesis*. Texas A&M University.

Willoughby, H. E. (1990). Temporal changes of the primary circulation in tropical cyclones. *Journal of the Atmospheric Sciences*, *47*(2), 242–264. https://doi.org/10.1175/1520-0469(1990)047<0242:TCOTPC>2.0.CO;2

Willoughby, H. E., Clos, J. A., & Shoreibah, M. B. (1982). Concentric eyewalls, secondary wind maxima, and the development of the hurricane vortex. *Journal of the Atmospheric Sciences*, *39*(2), 395–411. https://doi.org/10.1175/1520-0469(1982)039<0395:CEWSWM>2.0.CO;2

Xie, T., Wu, L. G., Feng, Y. C., & Yu, J. H. (2024). Alignment of track oscillations during tropical cyclone rapid intensification. *Advances in Atmospheric Sciences*, *41*(4), 655–670. https://doi.org/10.1007/s00376-023-3073-y

Yu, C.-L., Tang, B., & Fovell, R. G. (2023). Tropical cyclone tilt and precession in moderate shear: Precession hiatus in a critical shear regime. *Journal of the Atmospheric Sciences*, *80*(3), 909–933. https://doi.org/10.1175/JAS-D-22-0200.1

Yu, C.-L., Tang, B., & Fovell, R. G. (2024). Tropical cyclone boundary layer asymmetries in a tilt-following perspective. *Journal of the Atmospheric Sciences*, *81*(9), 1543–1563. https://doi.org/10.1175/JAS-D-23-0178.1

Zawislak, J., Jiang, H., Alvey, G. R., Zipser, E., Rogers, R., Zhang, J., & Stevenson, S. (2016). Observations of the structure and evolution of Hurricane Edouard (2014) during intensity change. Part I: Relationship between the thermodynamic structure and precipitation. *Monthly Weather Review*, *144*(9), 3333–3354. https://doi.org/10.1175/MWR-D-16-0018.1

Zhang, D.-L., Liu, Y., & Yau, M. K. (2001). A multiscale numerical study of Hurricane Andrew (1992). Part IV: Unbalanced flows. *Monthly Weather Review*, *129*(1), 92–107. https://doi.org/10.1175/1520-0493(2001)129%3C0092:AMNSOH%3E2.0.CO;2

Zhang, J. A., & Rogers, R. F. (2019). Effects of parameterized boundary layer structure on hurricane rapid intensification in shear. *Monthly Weather Review*, *147*(3), 853–871. https://doi.org/10.1175/MWR-D-18-0010.1

Zhang, J. A., Cione, J. J., Kalina, E. A., Uhlhorn, E. W., Hock, T., & Smith, J. A. (2017). Observations of infrared sea surface temperature and air-sea interaction in Hurricane Edouard (2014) using GPS dropsondes. *Journal of Atmospheric and Oceanic Technology*, *34*(6), 1333–1349. https://doi.org/10.1175/JTECH-D-16-0211.1

Zhang, J. A., Dunion, J. P., & Nolan, D. S. (2020). In situ observations of the diurnal variation in the boundary layer of mature hurricanes. *Geophysical Research Letters*, *47*(3), e2019GL086206. https://doi.org/10.1029/2019GL086206

Zhang, J. A., Rogers, R. F., & Tallapragada, V. (2017). Impact of parameterized boundary layer structure on tropical cyclone rapid intensification forecasts in HWRF. *Monthly Weather Review*, *145*(4), 1413–1426. https://doi.org/10.1175/MWR-D-16-0129.1

Zhang, Z., Zhang, W., Zhao, W., & Zhao, C. (2020). Radial distributions of sea surface temperature and their impacts on the rapid intensification of Typhoon Hato (2017). *Atmosphere*, *11*(2), 128–151. https://doi.org/10.3390/atmos11020128